SIMULATION OF COMBUSTION NOISE

OF PREMIXED FLAMES IN OPENFOAM

By

ANDREW J. WILLIAMSON

Bachelor of Science in Mechanical Engineering

Oklahoma State University

Stillwater, OK

2019

Submitted to the Faculty of the
Graduate College of the
Oklahoma State University
in partial fulfillment of
the requirements for
the Degree of
MASTER OF SCIENCE
May, 2022

SIMULATION OF COMBUSTION NOISE

OF PREMIXED FLAMES IN OPENFOAM

Thesis Approved:

Dr. Khaled Sallam

Thesis Adviser

Dr. Brian Elbing

Dr. Omer San

ACKNOWLEDGEMENTS

I would like to thank my family for tolerating my desires to continue my education and for providing me with loving respite during this long process. I would thank my advisor Dr. Khaled Sallam, for his continued support and encouragement. I would like to thank Dr. Brian Elbing and Dr. Omer San for serving on my graduate committee. I would like to thank Rheem for funding my graduate research and this thesis and Dr. Shubham Srivastava (Rheem) for his knowledge of CFD and combustion. I want to thank Umicore for their generous donation of the equipment used to build my experiment. I'd also like to thank John Shadley (J R Shadley Acoustics) for his knowledge of acoustics and allowing a student he barely knows to borrow his SPL meter.

Name: ANDREW J. WILLIAMSON

Date of Degree: MAY, 2022

Title of Study: SIMULATION OF COMBUSTION NOISE OF PREMIXED FLAMES IN OPENFOAM

Major Field: MECHANICAL AND AEROSPACE ENGINEERING

Abstract: Advancements in combustion which have increased efficiency and reduced greenhouse gas emissions, such as premixed combustion and lean injection, have led to increased noise emission due to higher turbulence and mixing fluctuations. This study explored the viability of a hybrid CFD and acoustic analogy method for simulating noise in residential furnaces. This was done by exploring the validity of various chemical mechanisms to reduce computational time requirements, validating the acoustic analogy in enclosed spaces with an expansion chamber silencer, and finally testing the method on a laboratory scale furnace geometry. The WD2, SG35, Z42, DRM22 and GRI-3.0 combustion mechanisms were compared against the experimental data of the Sandia D Flame. The computational cost of these mechanisms had a power relation to the number reaction as predicted by theory, except for the global mechanism which performed worse than both the skeletal mechanisms. The libAcoustics library and Ffwocs-Williams Hawkings (FWH) acoustic analogy was validated for confined flow using the expansion chamber silencer and plane wave-theory. The calculated transmission loss compared well with the plane-wave theory and the sine-sweep method was determined to be an effective method for simulating the acoustic source. Larger time steps smoothed the sound pressure level (SPL) frequency spectrum, but this did not result in a significantly depressed the overall sound pressure level (OASPL). A laboratory scale furnace was built, and the SPL frequency spectrum was measured with SPL meter and microphones. The equivalence ratio and ramping the flow rate did not significantly alter the SPL spectrum or OASPL. However, the flow rate had a linear relationship with the SPL amplitude and peak frequencies. A simulation of the laboratory scale furnace was performed using both LES and URANS turbulence modeling. The LES-FWH simulation of the furnace predicted the combustion peak frequency and amplitude, and the OASPL. The URANS simulation underpredicted the amplitude of the SPL spectrum.

TABLE OF CONTENTS

Chapter Page

LIST OF TABLES

Table Page

LIST OF FIGURES

Figure Page

Figure Page

Figure Page

Figure Page

CHAPTER I

INTRODUCTION

1.1 - Combustion Noise

1.1.1 - Introduction

When one thinks of pollution, likely chemical pollution will come to mind. However, noise pollution is more likely to have an immediate impact on nearby observers. Noise pollution can cause physical and psychological harm, as well as structural damage to nearby property. Acoustic resonations cause damage to the device in question, notably in the development of the Saturn rockets, the first manned missions to the moon. In the past, these issues were eliminated with costly trial and error experimentation, leading to a need to understand the underlying physics of combustion noise and develop models for combustor design [1].

Since combustion noise is a major issue in jet engines, most of the literature focuses on aircraft and rocket engines, however the work is also important for fields ranging from large scale furnaces to residential heating and hot water systems. All practical combustors are turbulent because the heat transfer is greater than that of a laminar system. Advancements in combustion which have increased efficiency and reduced greenhouse gas emissions, such as premixed combustion and lean injection, have led to increased noise emission due to higher turbulence and mixing fluctuations.

These advanced combustion techniques are becoming more popular as emission standards for residential heating systems are becoming stricter. Water heaters are closed vessels comprising of many pipes of small dimensions and are particularly prone to combustion driven acoustic oscillations. Most of the water heaters, especially tankless designs, involve intricate internal geometries along with premixed or partially premixed burners. As this equipment is installed inside the home premises near the living spaces, this noise can be a source of significant discomfort. Careful design of the combustion assembly is the key. Combustion entails fluctuations in the pressure field. Without proper acoustic design, these perturbations often find their way back to the combustion source after getting reflected from the chamber walls thus disrupting the heat release owing to variations in fuel flow or the combustible mixture.

It is generally agreed that noise from combustion is caused by fluctuations of the heat release rate of the system. This is caused by two different mechanisms known as direct and indirect noise [2]. Direct noise is related to the inherent unsteadiness of turbulent combustion, and the heat release fluctuations caused by the reactive region. Indirect noise, sometimes referred to as entropy noise, is generated when the non-uniform flow field interacts with the boundaries of the system. The relative impact of direct and indirect noise is still under contention, though it is agreed to be a function of the system geometry and conditions.

The subject of combustion noise has been studied for decades. The first and most widely cited paper, Strahle 1978 [1], focuses on combustion noise from open turbulent flames. Candel et al. 2008 [2], updated these accounts and included effects of confinement and a review of the state-of-the-art computational combustion acoustics (CCA) of the time. In 2015, Dowling and Mahmoudi [3] wrote of a review of recent progress and included more work on indirect combustion noise. Ihme 2017 [4] expanded on the subject and considered the impact on jet noise. Tam et al. 2019 [5], reviewed the advances in computational methods for modeling and prediction of combustion noise.

1.1.2 – Physical Description

In nearly every discussion of combustion noise, the experiment conducted by Thomas and Williams in 1966 [6] is used as a starting place to describe the physics of combustion noise. In the experiment, a soap bubble was filled with a homogeneous mixture of fuel and air. The bubble was ignited by a spark at the center. At a constant pressure, the combusting gas increased in volume which in turn emitted a pressure wave as shown in Figure 1.1. The measured pressure fluctuation, $p'(\vec{r},t)$, was proportional to the increase in the volume of the bubble in the following form:

$$p'(\vec{r},t) = \frac{\rho_\infty}{4\pi r}\left(\frac{\mathrm{d}^2 V}{\mathrm{d}t^2}\right) \tag{1.1}$$

where ρ_∞ is the farfield density, $\vec{r}$ is the distance from the flame source to the observer, V is the volume increase due to heat release. This is known as a monopole point radiator. The key point of Equation 1.1 is the noise is being generated by fluctuations in the rate of change of the volume.

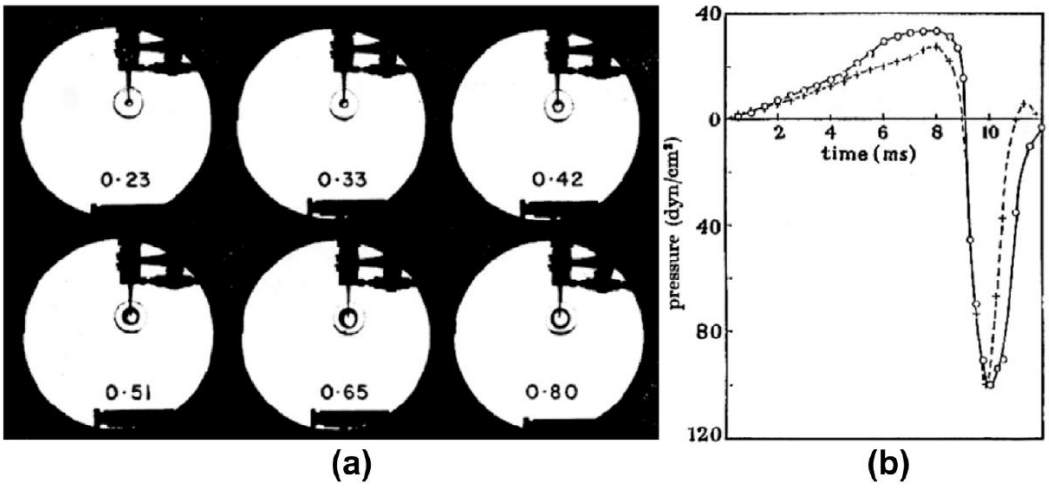

Figure 1.1 - (a) The spherical bubble expanding with time after ignition and (b) the acoustic pressure as a function of time: (+) for the measured quantity and (o) for the calculated value. [6]

Further, it was postulated that turbulent flames were a collection of eddies, each acting as a monopole point radiator. Experiments [7] were carried out to validate the theory assuming that a turbulent flame is an ensemble of monopole point radiators with varying frequency and strength distributed along the reacting zone. It was shown that pressure fluctuations are proportional to the rate of change of the volume of the reacting gasses. This volume is proportional to their consumption as shown in Equation 1.2.

$$p'(\vec{r},t) = \frac{\rho_\infty}{4\pi r}\left(\frac{\rho_u}{\rho_b} - 1\right)\left(\frac{\mathrm{d}^2 v}{\mathrm{d}t^2}\right) \tag{1.2}$$

where ρ_u and ρ_b are the densities of the unburnt and burnt gasses respectively, and v is the volumetric rate of consumption of the reacting gasses. In the case of lean premixed combustion, the volumetric rate of consumption is linearly proportional to the light emission intensity, *I*. This relationship has been used to estimate combustion noise and heat release rate, by measuring the emission intensity of the reacting region.

Using Lighthill's analogy [8,9] for aerodynamic sound and the governing laws of fluid mechanics one can derive an expression for the far-field sound from combustion region [10]:

$$p'(\vec{r},t) = \frac{\gamma-1}{4\pi r c_\infty^2}\int_{V_c} \frac{\partial \dot{Q}}{\partial t}(\vec{r}_0, t^*)\, dV(\vec{r}_0) \tag{1.3}$$

where γ is the specific heat ratio, *c* is the speed of sound in the combusted gas, $\vec{r}_0$ is the distance between the flame source and the noise source, and $\dot{Q}$ is the volumetric heat release rate in the combustion volume, V_C. Also, $t^* = t - |\vec{r} - \vec{r}_0|/c_\infty$ accounts for the time delay due to location of the observer from the various noise sources inside the combustion region. If the flame is assumed too small compared to the observer's distance $\vec{r} \ll \vec{r}_0$, then expression for time delay can be further simplified to $t^* = t - |\vec{r}|/c_\infty$.

Equation 1.3 is considered a primary result of combustion noise theory. The far-field pressure fluctuation forms as a result of the changes in the heat release rate of the combustion region. An expression for the mean square of the pressure fluctuation can be derived from Equation 1.3 which is a function of the mean square of the heat release rate and a correlation volume. This shows that to model the combustion of turbulent flames, one is required to model these two values properly.

1.2 – Computational Combustion Acoustics (CCA)

1.2.1 - Introduction

Computational Combustion Acoustics (CCA) is a relatively new field, and it uses many tools from the CAA and CFD (flame dynamics) fields. There are two main problems in the CCA field:

1) Determining the source of noise, which requires modeling small scale structures.

2) Modeling sound propagation into the far-field, of which the dimensions are generally orders of magnitude larger than the combustion region.

Since the computation domain sizes are completely different, calculating both problems in the same model is not a reasonable solution. Though there have been some studies where it was attempted, generally the two problems are dealt with separately.

The acoustic power of a flame is proportional to the density, nozzle diameter, laminar flame speed, and jet exit velocity. The scales of unsteady combustion are [4]:

$$Ma\lambda \sim \xi L \sim l_t \sim Re_t^{\frac{3}{4}} \eta \sim Re_t^{\frac{3}{4}} Ka^{-\frac{1}{2}} \delta_F \tag{1.4}$$

where Ma is the Mach number, λ is the acoustic wavelength, L is the characteristic flame length, l_t is the turbulence integral length scale, η is the Kolmogorov length scale, Ka is the turbulent Karlovitz number, and δ_F is the flame thickness. These scales are depicted in Figure 1.2.

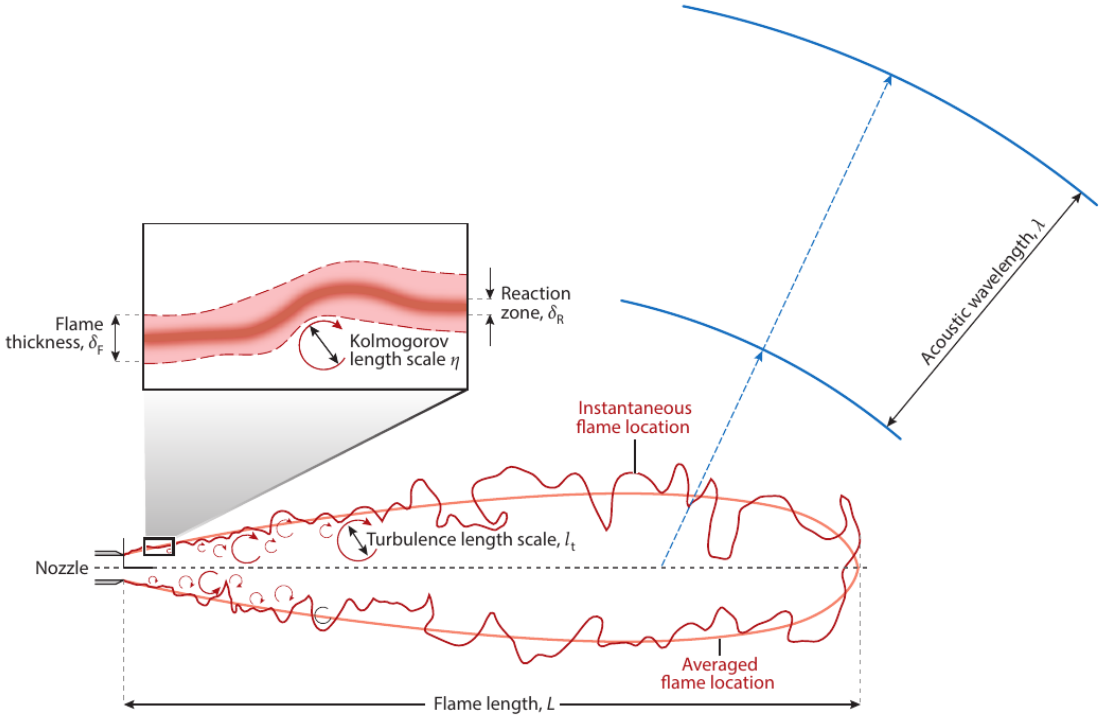

Figure 1.2 - Characteristic scales of a turbulent jet flame [4]

CAA techniques can be categorized in three main groups: empirical models, direct computation, and hybrid computation. The direct approach solves the sound by solving the compressible flow equations and the simulation must be sufficiently large to include the source of the noise and part of the near field. The hybrid approach decouples the sound calculations from the flow calculations. The far-field sound is obtained by the solution of an acoustic analogy using the computed source field data. This method assumes that the flow generates sound, but the sound does not affect the flow significantly. This means that the approach is only valid for low fluctuating Mach numbers.

Acoustic waves also have small amplitudes requiring low numerical noise and high frequencies with large wavelengths require small grid sizes to resolve. The long propagation distance means you must have minimal numerical dispersion and dissipation. Acoustic waves decay slowly and usually reach the boundaries of a finite computational domain requiring special consideration in

the boundary conditions to avoid reflection. The length scales of the acoustic wavelength are significantly different from the acoustic source [11]. The difference in scale for fluid and acoustic disturbances requires high numerical accuracy in the direct method, but with the hybrid approach numerical accuracy in the flow is less critical allowing for lower-resolution schemes [12].

1.2.2 – Empirical Models

Empirical models have been generated from experimental data collected throughout the years, though mainly for aircraft noise. GE [13] and Pratt and Whitney [14] developed semi-empirical tools for total acoustic power, which showed good agreement with data from the respective manufacturers but no other companies. SAE adopted the method developed by GE as a technical standard in 1980. The NASA Aircraft Noise Prediction Program (ANOPP) [15,16] later developed this method into what is now known as simply the SAE method.

1.2.3 – Direct Method

Direct methods use the physical model to calculate the sound generation from direct combustion and the surrounding field effects. This method reduces the number of approximations used by retaining the relationships between the various acoustic sources. However, a wide range of scales (Eq 1.1) are required to be included which makes simulations more challenging. One issue is the fact that some acoustic sources are not in the primary combustion regions, which would increase the meshing requirements. Also, a problem is the difference in time scales between the fluid and acoustic mechanisms. Direct numerical simulations have improved the knowledge of combustion by providing a detailed view of flame behavior [17]. It is also a useful tool in validating combustion models.

1.2.4 – Hybrid Methods

Hybrid Models are a variety of methods to represent the acoustics in the unsteady combustion including acoustic analogies, scale separation, and flow-field decomposition, many of which were originally developed for computational aero-acoustic applications (CAA) and converted to be used in combustion. Acoustic analogies are generally derived from the conservation equations and arranged into acoustic wave equations. Sources of combustion noise can be determined by using CFD combustion tools, then you can define methods for the propagation of the sound to the far-field. In confined flows, the sound propagation must be simulated over a large domain, which covers a few wavelengths. Indirect or hybrid schemes generally use LES simulations to calculate the fluctuations then in the second step the sound radiation using perturbed Euler equations. The far-field noise can also be determined by extrapolation of the nearfield values. Lighthill's acoustic analogy is commonly used, however, there are several other analogies, each of which account for different effects.

1.3 – Problem Statement

Commercially the process of reducing noise is done with an iterative design process. The process can be costly and time consuming to employ. With the advancements in the efficiency of computational fluid dynamics (CFD) the iterative design process can be aided by simulation. For noise reduction this requires a reliable method for testing noise levels for varying geometries. This study explored the viability of a hybrid CFD and acoustic analogy method for simulating noise in residential furnaces. This was done by exploring the validity of various chemical mechanisms to reduce computational time requirements, validating the acoustic analogy in enclosed spaces with an expansion chamber silencer, and finally testing the method on a laboratory scale furnace geometry.

1.4 – Specific Objectives

- Provide relevant background information in combustion and Acoustic Analogies
- Provide a brief description of the OpenFOAM software
- Provide information on combustion and acoustic implementation in OpenFOAM
- Validate various chemical mechanisms and compare their computational efficiency
- Validate the libAcoustics library using the expansion chamber silencer
- Build and measure the noise of a laboratory scale furnace
- Simulate the noise using OpenFOAM and the libAcoustics library
- Compare the acoustic noise from the experimental and simulated furnaces.

CHAPTER II

COMBUSTION AND ACOUSTIC MODELING IN OPENFOAM

2.1 – OpenFOAM

2.1.1 – Introduction to OpenFOAM

CFD simulations were performed using OpenFOAM, an object-oriented library written in C++ programming language, originally developed [18] in 1998. OpenFOAM is an open-source software with a large user base from both academic and commercial organizations. It uses the finite volume method (FVM) for solving the governing equations for CFD. The fork of OpenFOAM v2012 was used, which was developed by ESI OpenCFD Ltd [19]. ParaView [20], an open-source data analysis tool, is utilized for visualization and post-processing of the computational results. The benefit of using OpenFOAM compared with commercial software is the customizability and community. With OpenFOAM you can take an existing version and modify it to fit your specific needs and you can take advantage of rapid advances made by the CFD community without having to code new methodology.

2.1.2 – Time Directory

The results from OpenFOAM simulations are stored in the time directories. The initial time directory *0*, contains the files with boundary and initial conditions for the simulation. In this directory are files for each of the solvers required quantities such as the pressure, *p*, temperature,

T, velocity *U*, specie mass fraction *Y*, and turbulent properties. The required files are dependent on the solver used and the turbulence method used. After the simulation begins, the results are saved to new time directories named based on the time or iteration.

2.1.3 – Constant Directory

The constant directory contains the mesh, physical, and thermal properties of the simulation. The required files are dependent on the case, but most will contain the *polyMesh*, *turbulenceProperties*, and *thermophysicalProperties*. The constant directory also contains files with information about radiation, which was not considered here, as well as chemical reaction modeling information and the *fvOptions* described in section 2.2.

The *polyMesh* directory contains the mesh. It includes several files with information about the mesh including the *boundary, faces, neighbor,* and *points.* These are generated using either one of the included meshing software such as *blockMesh*, *snappyHexMesh*, *cfMesh*, or by porting the mesh from another software using the OpenFOAM utilities such as *fluentMeshToFoam*. The utility *blockMesh* is the most basic utility which breaks down the geometry into a set of hexahedral blocks. These blocks can be manipulated to create more complex geometries such as curves with some effort. The utility *snappyHexMesh* utilized a surface file (.stl) located in the *triSurface* folder to automatically generate a mesh that "snaps" to the surface file. This requires an initial *blockMesh* generated mesh to use as a base. Similarly, the utility *cfMesh*, included in some versions of OpenFOAM, automatically generates a mesh based on a surface file that has been converted (.fms) using the *surfaceFeatureEdges* utility. The *cfMesh* utility is simpler and easier to use but does not work well with all geometries since it does not have the variety of options of *snappyHexMesh*. The *snappyHexMesh* is highly customizable making it ideal for complex meshes, but also making it more difficult to use.

The *turbulenceProperties* file contains, as expected, the values for the turbulence for the simulation. Here the turbulence modeling is specified under *simulationType*, such as laminar or RAS for Reynolds Averaged Navier Stokes (RANS). More specific model characteristics are specified such as the closure model and relevant coefficients.

The *thermophysicalProperties* file contains the information to construct the thermophysical model. For reacting flows, it also has keywords relating to the chemistry of the simulation: *inertSpecie*, *chemistryReader*, *foamChemistryFile*, and *foamChemistryThermoFile*. The chemistry files contain the information regarding the chemical mechanisms described further in section 2.2.

2.1.4 – System Directory

The system directory files contain parameters associated with the solution and meshing procedures. The dictionary files for meshing are in the system directory named *blockMeshDict*, *snappyHeshMeshDict*, and *meshDict* (for *cfMesh*). The file *meshQualityDict* and *surfaceFeatureExtractDict* are optional dictionaries for use with the *snappyHexMesh* utility.

The *controlDict* dictionary contains the runtime control parameters including the start time, end time, time stepping controls, solution write controls. The time stepping can be controlled as constant or based on a maximum courant number. The *controlDict* also has a function dictionary that allows for additional functions to operate on each iteration. These functions include calculating additional fields or sampling fields. Also, additional libraries such as *libAcoustics* described in section 2.3 may be implemented using the function dictionary.

The case solution parameters are in the files *fvSchemes* and *fvSolution.* The *fvSchemes* dictionary contains the numerical schemes used for solving the time, gradients, and divergence quantities. These schemes are limited to first and second order schemes in the main branches of OpenFOAM, however, some other branches do contain higher order schemes. The *fvSolution* file contains the equation solvers, tolerances, and algorithms. The algorithms available are the

pressure-implicit split-operator (PISO) or semi-implicit method for pressure-linked equations (SIMPLE) algorithms. These algorithms are the procedures for solving velocity and pressure, PISO for transient and SIMPLE for steady state. Additionally, the PIMPLE algorithm is a combination of the two with the option for transient or steady state depending on the solution settings.

Dictionary files for other OpenFOAM utilities are in the system directory as well. A couple useful utilities are the *setFields* and *topoSetDict* utilities. The *setFields* utility customizes the initial quantities of the fields. The *topoSetDict* utility creates sets of cells, faces, and more, for use in post processing or real time processing of quantities. It also allows for energy to be added to the system which is important for combustion ignition in cases where there is no pilot flame.

2.2 – Modeling Reacting Flow

2.2.1 – Governing Equations

The governing equations for reacting flows do not vary greatly from the standard system [21]. There is no mass generation in reacting flows, so the conservation of mass is the same as that for non-reacting flows.

$$\frac{\partial \rho}{\partial t} + \frac{\partial (\rho u_i)}{\partial x_i} = 0, \tag{2.1}$$

where ρ is the density, u is the velocity, and t is the time. When dealing with low velocity flow (Ma < 0.3) it is generally assumed that the compressibility effects are negligible, and the density is assumed constant. For combustion cases the density can change significantly due to chemical reactions. In the case of acoustic modeling, it is also important to model the changes in density.

For reacting flows, the individual species mass conservation must also be calculated.

$$\frac{\partial (\rho Y_k)}{\partial t} + \frac{\partial}{\partial x_i}\left(\rho u_i Y_k - \rho D_k \frac{\partial Y_k}{\partial x_i}\right) = \dot{\omega}_k, \qquad \text{for } k = 1, N \tag{2.2}$$

where Y_k is the species mass fraction, D_k is the diffusivity of species k, and $\dot{\omega}_k$ is the species reaction rate.

The conservation of momentum for reacting flows can be expressed as:

$$\frac{\partial}{\partial t}(\rho u_i) + \frac{\partial}{\partial x_i}(\rho u_i u_j) = -\frac{\partial p}{\partial x_i} + \frac{\partial \tau_{ij}}{\partial x_i} + \rho \sum_{k=1}^{N} Y_k f_{k,j} \tag{2.3}$$

where p is the pressure, $f_{k,j}$ are the forces acting on species k in direction j, and τ_{ij} is the stress tensor:

$$\tau_{ij} = \mu \left(\frac{\partial u_j}{\partial x_i} + \frac{\partial u_i}{\partial x_j}\right) - \frac{2}{3}\mu \frac{\partial u_k}{\partial x_k}\delta_{ij} \tag{2.4}$$

where μ is the dynamic viscosity estimated with the Sutherland formula [22].

The conservation of energy can be written in terms of sensible enthalpy which is applied often in CFD due to the ease of implementation. The transport equation for sensible enthalpy, h_s, is simplified to:

$$\frac{\partial \rho h_s}{\partial t} + \frac{\partial \rho u_i h_s}{\partial x_i} = \frac{Dp}{Dt} + \frac{\partial}{\partial x_i}\left(\alpha \frac{\partial h_s}{\partial x_i}\right) + \dot{\omega}_T \tag{2.5}$$

where α is the thermal conductivity and $\dot{\omega}_T$ heat release rate.

Additionally thermodynamic equations of state are used to close the system of equations. The ideal gas assumption is made to calculate density and to develop a relationship between enthalpy and temperature.

$$\rho = \frac{P \sum_{k=1}^{N} Y_k MW_k}{\bar{R}T} \tag{2.6}$$

$$h_s = \int_{T_0}^{T} c_p dT \tag{2.7}$$

The JANAF thermochemical tables [23] are used to calculate the heat capacity c_p in Eq 2.6.

$$c_p(T) = \bar{R}(a_0 + a_1T + a_2T^2 + a_3T^3 + a_4T^4) \tag{2.8}$$

2.2.2 – Chemical Reactions

Modeling the chemical reaction rate is a crucial part of reacting flows [21]. For laminar flow, the reaction rate is explicitly controlled by chemistry. The following depicts a system with N species and O reactions:

$$\sum_{k=1}^{N} v'_{k,j} M_k \rightleftharpoons \sum_{k=1}^{N} v''_{k,j} M_k \tag{2.9}$$

where v'_{kj} and v''_{kj} are the stoichiometric coefficients of the reactants and products respectively and M is an arbitrary representation of the chemical species. In such a system the reaction rate can be expressed as:

$$\dot{\omega}_k = MW_k \sum_{j=1}^{O} v_{k,j} Q_j \tag{2.10}$$

where $v_{kj} = v''_{kj} - v'_{kj}$ and Q_j, the rate of progress of reaction j, is written:

$$Q_j = k_{fj} \prod_{k=1}^{N} \left(\frac{\rho Y_k}{MW_k}\right)^{v'_{kj}} - k_{rj} \prod_{k=1}^{N} \left(\frac{\rho Y_k}{MW_k}\right)^{v''_{kj}} \tag{2.11}$$

where k_{fj} and k_{rj} are the forward and reverse rates of reaction j, respectively. These reaction rates are generally modeled using the empirical Arrhenius Law [21]:

$$k_{f,j} = A_{f,j} T^{\beta j} \exp\left(-\frac{E_j}{RT}\right) \tag{2.12}$$

where A_f is the preexponential constant, β is the temperature coefficient, and E is the activation energy. The backwards rates are then computed from the forward rates using equilibrium constants. Reaction rates are generally written in CHEMKIN [24] format and form a set of ordinary differential equations. This is one of the most computationally expensive parts of combustion simulations, particularly for detailed chemical mechanisms. This comes back to the

current challenge of finding a chemical mechanism that is small enough to be computationally inexpensive but also properly describes the variables of interest.

2.2.3 – Turbulent Reaction Rate Modeling

One of the most popular models for turbulent reaction rate modeling in commercial codes is the Eddy Break Up Model (EBM) proposed by Spalding [25]. It assumes that the reaction rate is controlled by the turbulent motions rather than the chemistry and combines the energy and species equations. The EBM can compute the reactions of a high number of species much faster by avoiding the chemical kinetics. The model has shown good results for high Reynolds number premixed combustion, but it is not advisable for low Reynold's flow or diffusion and partially premixed flames since it does not include any effects of chemical kinetics [21]. The reaction rate for the EBM is:

$$\overline{\dot{\omega}_{\Theta}} = C_{EBU}\bar{\rho}\frac{\widetilde{\Theta}(1-\widetilde{\Theta})}{\tau_{EBU}} \tag{2.13}$$

where $\widetilde{\Theta}$ is the mean reduced temperature which is a function of the temperature and mass fraction, $\overline{\dot{\omega}_{\Theta}}$ is the mean reaction rate for the reduced temperature, C_{EBU} is the model constant of the order of unity, and τ_{EBU} is the characteristic turbulent mixing time. For RANS the characteristic turbulent mixing time, $\tau_{EBU} = k/\epsilon$ and for LES, $\tau_{EBU} \approx \Delta/\sqrt{k^{SGS}}$, where k is the turbulent kinetic energy, ϵ is the energy dissipation rate, and Δ is the filter size.

The eddy dissipation concept (EDC) [26] was a continuation of the EDM. EDC incorporates both turbulent mixing and chemical kinetics which allows it to be applicable to diffusion and partially premixed flames. It is based on the energy cascade, where energy is transferred from the largest to smallest eddies then dissipates into heat. Chemical reactions only take place in the fine turbulent structures which are assumed to be isobaric and adiabatic perfectly stirred reactors. The

fine turbulent structures are characterized by their mass fraction γ_λ and their characteristic time scale τ^* [27]. The mean reaction rate can be expressed as [28]:

$$\overline{\dot{\omega}_k} = -\frac{\bar{\rho}}{\tau^*}\frac{\gamma_\lambda^2}{1-\gamma_\lambda^2}(\tilde{y}_k - y_k^*) \tag{2.14}$$

where y_k^* is the mass fraction in the fine structures and $\tilde{y}_k$ is the mean mass fraction between the fine structures and the surroundings. The turbulent structures mass fraction and their time scale are derived from the Kolmogorov's theory [27]

$$\tau^* = C_\tau \left(\frac{\nu}{\epsilon}\right)^{1/2} \tag{2.15}$$

$$\gamma_\lambda = C_\gamma \left(\frac{\nu\epsilon}{k^2}\right)^{1/4} \tag{2.16}$$

where the constants were determined to be C_τ = 0.4083 and C_γ = 2.1377 for the most recent iteration of the method [29].

Since the EDC method assumes the entire cell is a perfectly mixed reactor the model required a fine grid resolution to resolve the flame thickness. To resolve this issue the Partially Stirred Reactor model (PaSR) [30,31] further builds on EDC by splitting each cell into reacting and non-reacting portions. After reactions occur, mixing begins for a mixing time:

$$\tau_{mix} = C_{mix}\sqrt{\frac{\mu_{eff}}{\rho\epsilon}} \tag{2.17}$$

where μ_{eff} is the effective dynamic viscosity. C_{mix} is the mixing constant and is usually set between 0.001 and 0.3, but can be estimated by [32]:

$$C_{mix} = \sqrt{\frac{1}{1+C_\mu Re_t}} \tag{2.18}$$

where $Re_t = k^2/\epsilon\nu$ is the turbulent Reynolds number and $C_\mu = 0.09$. The mean reaction rate is determined by:

$$\overline{\dot{\omega}_k} = \kappa\dot{\omega}_k \tag{2.19}$$

where the reacting mixture fraction κ is defined as:

$$\kappa = \frac{\tau_c}{\tau_c+\tau_{mix}} \tag{2.20}$$

where τ_c is the chemical time scale or the finite rate which is defined as:

$$\frac{1}{\tau_c} = -\frac{\partial\dot{\omega}_k}{\rho\partial Y_k} \tag{2.21}$$

The PaSR model can use complex chemistry mechanisms incorporating both the turbulent and chemical reaction time scales. Unlike the EDC however, it can split each cell into reacting and non-reacting portions, which is advantageous for industrial applications where small cell sizes can make the simulation computationally expensive.

2.2.4 – Chemistry Modeling with *reactingFoam*

The solver reactingFoam is a transient compressible chemistry solver for mixing and combustion. It requires each incoming specie's mass fraction and boundary conditions to be specified in a separate file in the time directory. The boundary condition for species which are not incoming may be specified with a *Ydefault* file or a separate file for each specie.

The solver requires extra dictionaries in the constant directory to model the chemical reactions. The *chemistryProperties* file contains the chemical reaction ODE solver and its coefficients as well as the option to toggle the chemistry on or off and the initial chemical time step. The *combustionPropreties* file contains the combustion model and its coefficients.

The *foamChemsitryFile* contains the information about the chemical reactions and lists the species for the transport equations. The *foamChemistryThermoFile* contains the thermodynamic properties of the species and the Sutherland formula coefficients. The *foamChemsitryFile* and the *foamChemistryThermoFile* have an OpenFOAM specific format, however, the format of chemical mechanisms is generally given in CHEMKIN format. The *ChemkinToFoam* utility can be used to convert the mechanisms from CHEMKIN format to that required by OpenFOAM.

The chemical mechanism WD2 developed by Westbrook and Dryer [33], is a global mechanism using 6 species and 2 reactions:

$$CH_4 + \frac{3}{2}O_2 \rightarrow CO + 2H_2O \tag{2.22}$$

$$CO + \frac{1}{2}O_2 \rightleftharpoons CO_2 \tag{2.23}$$

The reaction mechanism was written in CHEMKIN format shown in Figure 2.1 then converted to OpenFOAM using the chemkinToFoam utility.

```
ELEMENTS
O H C N
END
SPECIES
CH4 O2 CO H2O CO2 N2
END
REACTIONS
CH4 + 1.5 O2 => CO + 2H2O 1.59E13 0 47.8E3!
FORD / CH4 0.7 /
FORD / O2 0.8 /

CO + 0.5 O2 <=> CO2 + 0H2O 3.98E14 0 40.7E3!
REV /5E8 0 40.7E3/
FORD / CO 1.0 /
FORD / O2 0.25 /
RORD / H2O 0.5 /
RORD / CO2 1 /

END
```

Figure 2.1 - CHEMKIN file for the WD2 reaction mechanism.

Ignition can be achieved in flames without pilots with the use of *fvOptions* dictionary. The option *energySource* can be used to inject energy into a set of cells specified with the *topoSetDict*.

2.3 – Acoustic Modeling

2.3.1 – Acoustic Analogies

The *libAcoustics* [34] library is an add-on for OpenFOAM. It was developed for far-field noise computation and contains predictions using the Curle analogy [35], Ffwocs Williams Hawkings analogy (FWH) [36], and CFD-BEM coupling. The *libAcoustics* library contains formulations for the FWH analogy: Farassat 1A formulation (1A) [37] and Garrick Triangle formulation (GT) [38]. The acoustic pressure is a sum of the monopole, dipole, and quadrupole non-linear sources.

$$p'(\vec{x},t) = p'_T(\vec{x},t) + p'_L(\vec{x},t) + p'_Q(\vec{x},t) \tag{2.24}$$

where the subscript T, L, and Q denote thickness, loading, and quadrupole respectively.

The 1A formulation contains the assumption that the control surface surrounds all non-linear sources making their contribution approach zero. The thickness and loading noise components of the 1A formulation are:

$$\begin{aligned} 4\pi p'_T(\vec{x},t) = &\int_{f=0}\left[\frac{\rho_0 \dot{v}_n}{r(1-M_r)^2} + \frac{\rho_0 v_n \hat{r}_i \dot{M}_i}{r(1-M_r)^3}\right]_{ret} dS \\ &+ \int_{f=0}\left[\frac{\rho_0 c v_n (M_r - M^2)}{r^2(1-M_r)^3}\right]_{ret} dS \end{aligned} \tag{2.25}$$

$$\begin{aligned} 4\pi p'_L(\vec{x},t) = &\int_{f=0}\left[\frac{\dot{\rho}\cos\theta}{cr(1-M_r)^2} + \frac{\hat{r}_i \dot{M}_i p\cos\theta}{cr(1-M_r)^3}\right]_{ret} dS \\ &+ \int_{f=0}\left[\frac{p(\cos\theta - M_i n_i)}{r^2(1-M_r)^2} + \frac{(M_r - M^2)\, p\cos\theta}{r^2(1-M_r)^3}\right]_{ret} dS \end{aligned} \tag{2.26}$$

In this formulation, ρ_0 is the reference density, $\vec{v}$ is the relative velocity, $\vec{r}$ is the distance from the sound source to the observer position $\vec{x}$, M is the Mach number, S is the surface area. The

subscript r represents the dot product of the vector and the distance $\vec{r}$, the subscript n designates the dot product of the vector with the unit normal vector $\hat{n}$.

The GT formulation is a special case of the 1A formulation in the 'wind tunnel' case where the source and observer are stationary with uniform flow. The formulation simplifications increase computational efficiency without loss of generality [39]. This simplification led to the formulation:

$$4\pi p_T'(x,t) = \int_{f=0}\left[\frac{\rho_0 \dot{v}_n}{R(1-M_R)^2}\right]_{ret} dS + \int_{f=0}\left[\frac{\rho_0 c v_n (M_R - M^2)}{R^2(1-M_R)^3}\right]_{ret} dS \tag{2.27}$$

$$4\pi p_Q'(\vec{x},t) = \int_{f=0}\left[\frac{\dot{\rho}\cos\theta}{R(1-M_R)^2} + \frac{\hat{R}_i \dot{M}_i p \cos\theta}{R(1-M_R)^3}\right]_{ret} dS + \int_{f=0}\left[\frac{(M_R - M^2)\, p\cos\theta}{R^2(1-M_R)^3}\right]_{ret} dS \tag{2.28}$$

where R now represents the effective acoustic distance between the source and the observer. After calculating the time domain results, they can be converted to the frequency domain spectrum with the Fast Fourier transform (FFT). The amplitude of the FFT should be calculated. Then the pressure amplitudes in the frequency domain are converted into sound pressure level (SPL) with a reference pressure of $p_0 = 20$ μPa.

$$SPL = 20\log_{10}\left(\frac{p'(f)}{p_0}\right) \tag{2.29}$$

Replacing the sound pressure in Equation 2.26 with the root-mean-square (rms) sound pressure, as a function of time, the overall sound pressure level (OASPL) can be obtained.

2.3.2 – Acoustic Implementation with *libAcoustics*

The *libAcoustics* [34] library is not a standard library for OpenFOAM and requires separate installation. The library is available on GitHub for multiple versions of OpenFOAM and is currently being maintained by the UniCFD Web-laboratory [40]. The library is implemented by including the control files in the functions portion of the controlDict. The control file contains the analogy type and formulation, as well as relevant coefficients depending on the formulation. The control file also specifies the control surfaces used in the FWH analogy. The control file also includes the *commonSettings* file which contains other information that is common to all analogies, in case there are multiple analogies being implemented. The time settings, speed of sound, and observer locations as well as the reference velocity, pressure, and density are in the commonSettings file.

2.4 – Summary

A brief description of the OpenFOAM software and case structure for the version OpenFOAM v2012 was given in this chapter. Details on modeling reacting flows was given with an emphasis on chemical mechanism and turbulence modeling. The reactingFoam solver and its additional requirements were then described. Finally, the acoustic analogies in the libAcoustics library were described in the previous section along with the implementation of the libAcoustics library in OpenFOAM cases.

CHAPTER III

SANDIA D FLAME CHEMICAL MECHANISM COMPARISON

3.1 – Introduction

Methane is the primary combustive in biogas and the fossil fuel known as natural gas. Natural Gas is considered one of the most environmentally friendly fossil fuels since its combustion results in relatively few pollutants and it is easy to store, transport and use [41]. Natural Gas has become a widely used alternative for crude oils. According to the British Petroleum: Statistical Review of World Energy [42], Natural Gas accounted for 24.2% of the world's energy production, barely trailing that of oil and coal.

Also, since the molecule is relatively small and simple, methane combustion chemical kinetics is better understood when compared to more complex fuel such as diesel or gasoline. Methane has been the subject of many detailed chemical kinetic mechanisms and the most simplified kinetic mechanisms for computation fluid mechanics (CFD) simulations. Complex chemistry offers a detailed and accurate view of combustion however it requires large computational resources leading to the need for accurate less complex chemical mechanisms. As the implementation of CFD in industrial settings becomes more prevalent in the iterative design process, the need for reduced computational time often trumps the need for laboratory level accuracy [43].

Chemical mechanisms range from comprehensive detailed mechanisms with thousands of reactions, to global reaction mechanisms with only a few reactions. Comprehensive mechanisms were developed to accurately describe any combustion case. Chemical mechanisms known as detailed also include some with simplifications that make them less than comprehensive but reduce the number of reactions to a few hundred rather than thousands. Skeletal mechanisms restrict the comprehensiveness further but still contain an intact sequence of reactions from fuel to final product. Reduced mechanisms are a further simplification of skeletal mechanisms often using an automatic reduction strategy. Global and semi-global mechanisms only have only a few steps and are generally not able to accurately reproduce important combustion characteristics. Lu et al. [44] presented a review of the reaction mechanisms of fuel oxidation, the need for comprehensiveness of detailed mechanisms, and theories for reduction of detailed mechanisms. In detailed mechanisms there are a huge number of chemical reactions with computation cost that is a function of the reactions and therefore the number of species and even for small fuels like methane, detailed chemical mechanisms are too large for industrial scale computation. Curran [45] reviewed the development of these mechanisms, stating that the size of mechanisms increases with time and the ability for increased computational power (Figure 3.1a).

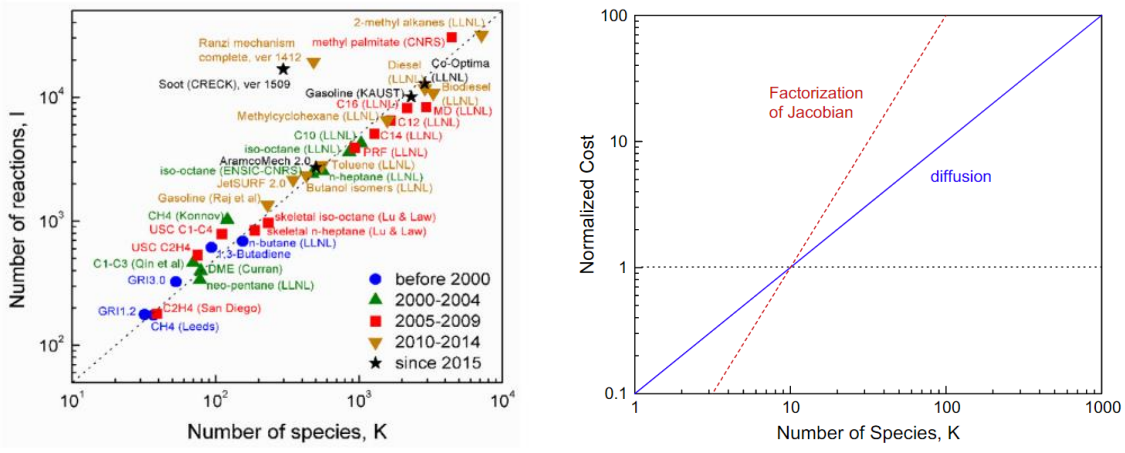

Figure 3.1 – (a) Chemical mechanisms for combustion shown with the reactions as a function of species. [45] (b) Computational cost of simulations as a function of the number of species. [44]

Zhang et al. 2021 [46] compared methane combustion mechanisms using shock tube and rapid compression machine ignition delay time measurements. Their study focused on detailed mechanisms. Laguillo et al. [47] compared global, skeletal, and detailed mechanisms for domestic gas cooking burners. They found that global mechanisms are not suitable for laminar flame speed, as well as overpredicting CO formation and fuel consumption. These results are important but leave room for analysis of a jet flame. Zettervall et al. [43] reviewed many kinetic mechanisms for methane with varying levels of complexity from 2 reactions to 5131 reactions. They tested the laminar burning velocity and ignition delay for a wide range of conditions. They found that the DRM22 mechanism with 104 reactions was in good agreement over a wide variety of conditions and recommended the Z42 as a good smaller mechanism.

These studies leave room for more evaluations of methane chemical mechanisms. The Sandia D Flame is a well-developed benchmark for turbulent partially premixed combustion, and it has been used in previous studies [48-51] for validating the combustion models in OpenFOAM. The present study aims to compare the accuracy and the computational cost of five chemical mechanisms that were selected because of their past performance and their relative sizes. The global mechanism WD2 with 2 reactions was compared with reduced and detailed mechanisms: SG35, Z42, DRM22, and GRI-30, with 35, 42, 104, and 325 reactions respectively.

3.2 – Computational Method

3.2.1 – Sandia Flame D

The Sandia piloted methane-air jet flames data sets [52,53] were provided online for comparisons of models and measured data. The burner geometry was developed by Sydney University [54]. Flame D, simulated in the study, is shown in Figure 3.2 on the left with a laser beam and on the right close-up view of the burner.

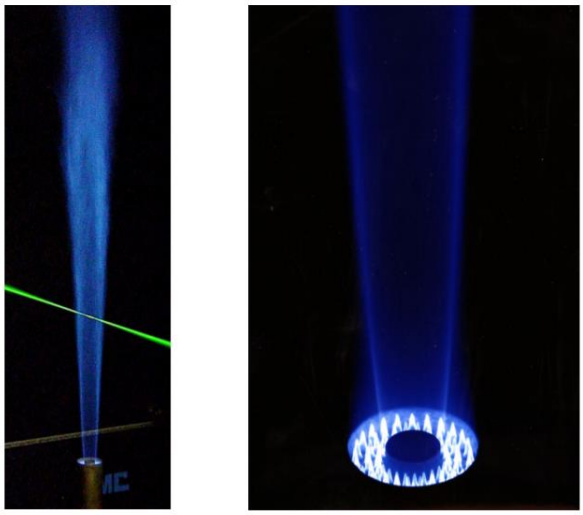

Figure 3.2 – Images of the Sandia D flame. (left) LIF measurements with a laser. (right) close-up of the burner outlet and pilot flames.

The jet was a premixed fluid 25% CH_4 – 75% Air by volume. The pilot was a mixture of C_2H_2, H_2, O_2, CO_2, and N_2. The burner was placed above the exit of a vertical wind tunnel to allow co-flow air. The dimensions of the burner are listed in Table 3.1.

Table 3.1 – Dimensions of the Sandia D flame and pilot flames.

Main Jet Diameter, D	7.2 mm
Pilot Inner Diameter, d_i	7.7 mm
Pilot Outer Diameter, d_o	18.2 mm
Burner Outer Diameter, D_o	18.9 mm

The main jet inlet conditions were U = 49.6 m/s and T = 294 K. The co-flow air inlet conditions were U = 0.9 m/s and T = 291 K. The pilot was measured at the exit of the burner for flame D, where the temperature measured to be T = 1880 K. The measured mass concentrations and the other relevant inlet conditions for the simulation are shown in Table 3.2.

Table 3.2 - Inlet conditions for the Sandia D Flame Simulation

	Specie	Y_k	U (m/s)	T (K)
Main Jet	CH_4	0.1561	(49.6 0 0)	294
	O_2	0.1966		
	N_2	0.6473		
Pilot	CO	4.07e-03	(11.4 0 0)	1880
	CO_2	0.1098		
	H	2.48e-05		
	H_2	1.29e-04		
	H_2O	0.0942		
	O	7.47e-04		
	O_2	0.0540		
	OH	0.0028		
	N_2	0.7342		
	NO	4.80e-06		
Coflow Jet	O_2	0.23	(0.9 0 0)	291
	N_2	0.77		

The data [54] from the Sandia Flame D include measured scalars: temperature, mixture fraction, and mass concentrations of N_2, O_2, H_2O, H_2, CH_4, CO, CO_2, OH, and NO. The data was measured using Raman scattering and LIF; the LIF measurements were considered more accurate. The data also included the Reynolds and Favre averaged mass fractions and rms fluctuations.

3.2.2 –Computational Grid

The computational domain was split axially and reduced into a wedge-shaped two-dimensional mesh. The two-dimensional mesh reduces the computational time required by assuming symmetry around the center axis. A five-degree portion of the computational domain is represented by the mesh. The smallest mesh size is shown in Figure 3.3 with 5170 cells.

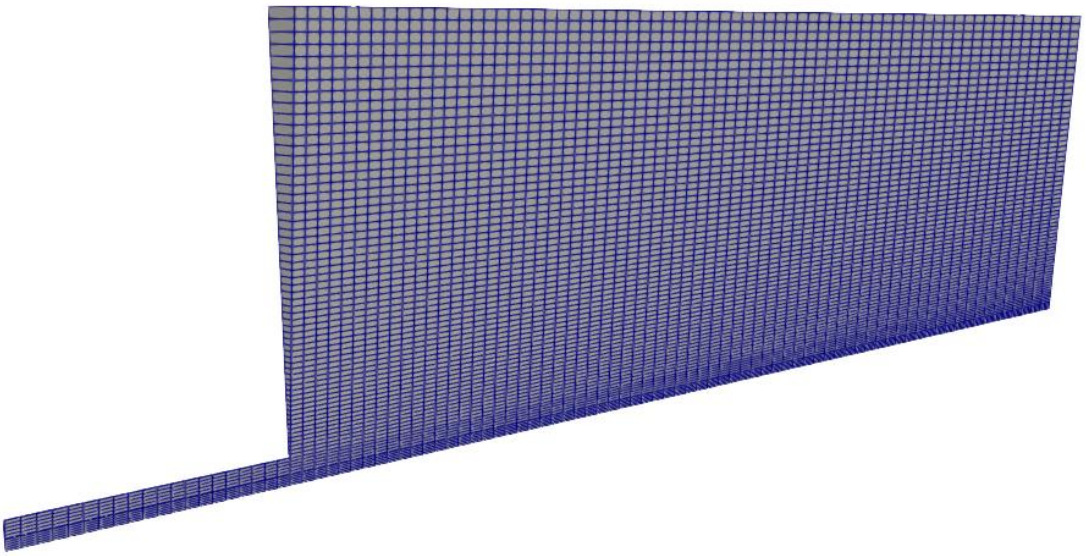

Figure 3.3 – Two-dimensional wedge mesh of a five-degree portion of the full Sandia D flame geometry.

The effects of mesh size on the accuracy of the simulation were determined by halving the cell height and width. The number of cells increased by approximately a factor of 4 at each stage however this is not exact due the geometry of the inlet. The number of cells were 5170, 20540, 81880 and are shown from left to right respectively in Figure 3.4.

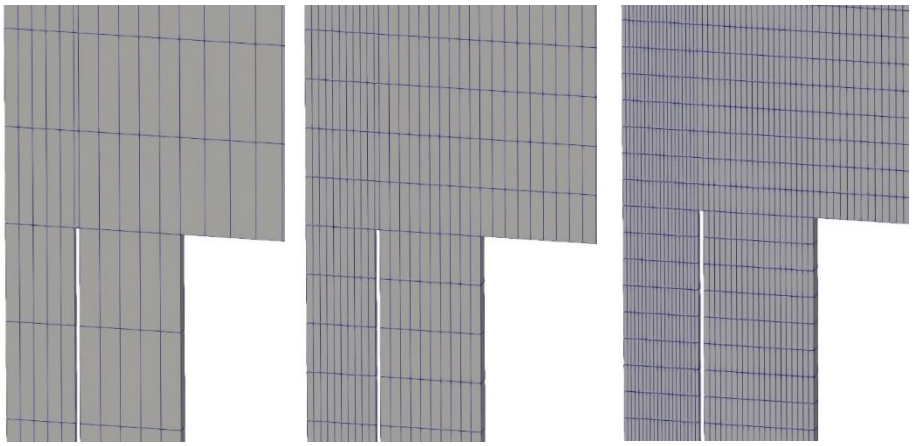

Figure 3.4 – Computational mesh size was compared at 5170, 20540, and 81880 cells. A small portion of the mesh is displayed here with increasing cell size from left to right.

3.2.3 – Chemical Mechanisms

Five chemical mechanisms were compared for their speed and accuracy in this study. One global mechanism proposed by Westbrook and Dryer [33] with two equations (WD2) was compared. Two skeletal mechanisms used were developed by Smooke and Giovangigli [55] with 35 equations (SG35) and another with 42 equations Z42 [56]. Two detailed mechanisms DRM22 [57] and GRI-3.0 [58] were also used with 104 and 325 reactions respectively. A summary of the species and reactions are listed in Table 3.3

Table 3.3 - Chemical mechanism reaction and specie summary

Mechanism	**WD2**	**SG35**	**Z42**	**DRM22**	**GRI-3.0**		
Reactions	2	35	42	104	325		
Species	6	16	18	22	53		
Additional Species	CH_4 CO CO_2 H_2O N_2 O_2	CH_2O* CH_3 CH_3O H H_2 H_2O_2 HCO HO_2 O OH	CH* CH2	AR C_2H_2 C_2H_3 C_2H_4 C_2H_5 C_2H_6 $CH_2(S)$ CH_2O	C C_2H C_3H7 C_3H8 CH_2O CH_2O H CH_3C CHO CH_3	OH CN H_2CN HCCO HCCO H HCN HCNN HCNO HNCO HNO	HOCN N N_2O NCO NH NH_2 NH_3 NNH NO NO_2

* Specie not in DRM22

3.2.4 - Simulation Settings

The simulation was performed in OpenFOAM utilizing the transient-compressible solver reactingFoam using the PIMPLE algorithm. The numerical settings are listed in Table 3.4. The simulation was performed using the local Euler time stepping method, a semi-steady state solution method that smooths the time steps between low and high computational regions. The computational domain was split using the scotch algorithm to run the system in parallel on 8 CPUs for the mesh study and 32 CPUs for the subsequent comparison study. Different ODEs

solution methods were compared; Euler Implicit was the first order accurate method and the semi-implicit mid-point solvers (SIBS) [59] was the second order method.

Table 3.4 – Sandia D Flame Simulation settings

PIMPLE	nOuterCorrectors nCorrectors	1 3
LocalEuler	rDeltaTSmoothingCoeff rDeltaTDampingCoeff	0.025 1
Solvers	rho p U|h|k|epsilon|Yi	Diagonal PCG|DIC PBiCGStab|DILU
Numerical Schemes	ddtSchemes gradSchemes divSchemes	localEuler linear limitedLinear 1

3.3 – Results and Discussion

3.3.1 – Computational Grid

The percent difference between the outlet and inlet mass and energy quantified convergence. The mass and energy (Figure 3.5) become stable around 15 thousand iterations for the two smaller mesh sizes. The largest mesh has oscillations occurring in both the mass and the energy balance.

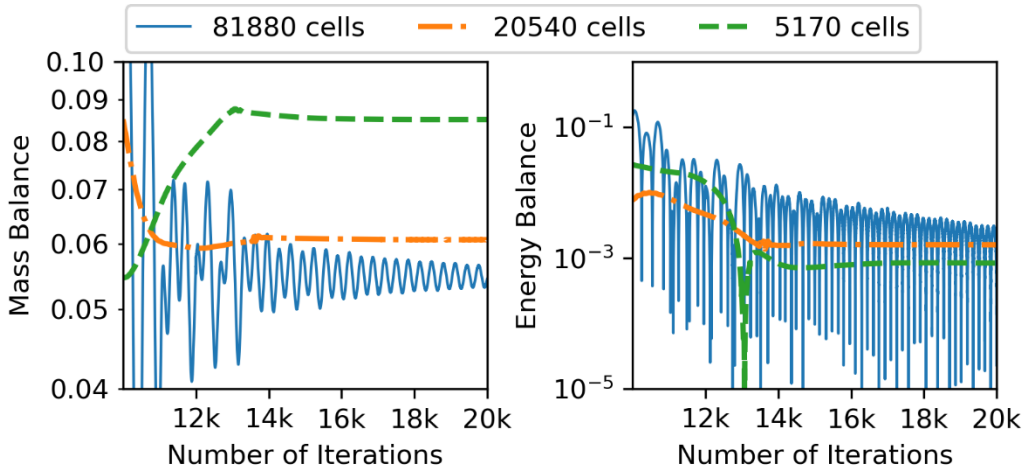

Figure 3.5 – The normalized (left) Mass Balance and (right) Energy Balance as a function of the number of iterations for increasing mesh sizes.

With increased cell count the computational cost increased as shown in Figure 3.6(a). Halving the size of the cell and increasing the number of two-dimensional cells by a factor of four increased the computational time by a factor of three. This may be due to the *localEuler* time stepping method that lessens the computational requirements in low velocity regions. After convergence, the percent difference between the inlet and outlet mass and energy was plotted as a function of the mesh size in Figure 3.6(b). The difference caused by the diffusion of the numerical methods employed decreases as the mesh size increases. The decrease in numerical diffusion in the continuity from the smallest to medium mesh is significant but less so for the next step. The energy balance did not significantly change from the small to medium mesh sizes with both having around 0.1%, though increasing to the next size decreased this to less than 0.01%.

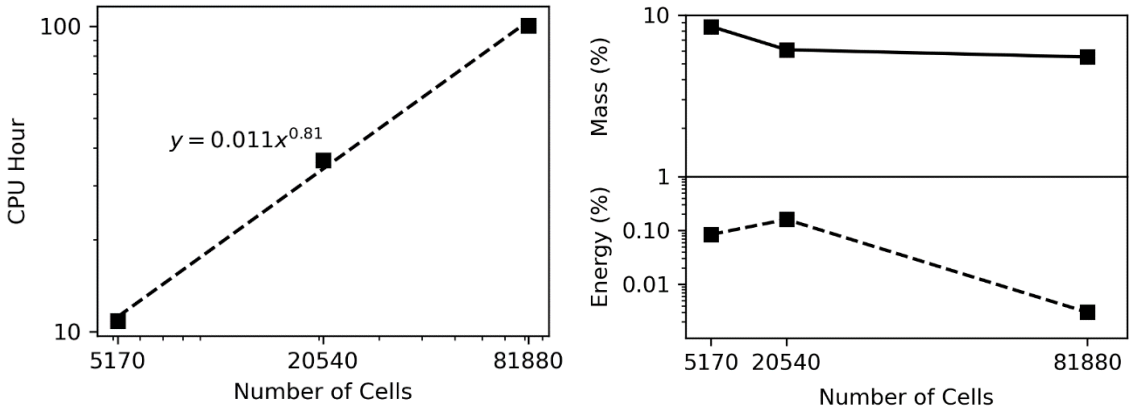

(a) (b)

Figure 3.6 - (a) Computational time and (b) converged mass balance and energy balance as a function of the mesh size.

The three cases were also compared to the Sandia D experimental data. The radial distribution of the mass fraction of methane and the temperature was plotted at 4 different distances from the outlet. The distances were multiples of the diameter, x/d = 30, x/d = 15, x/d = 7.5, and x/d = 3. The mass fraction CH_4 is shown in Figure 3.7(a). The mass concentration starts near the inlet value and decreases farther from the outlet as combustion is occurring. The larger cell sizes of the smallest mesh cause diffusion at a distance x/d = 3, closest to the outlet, and increased reaction

rate shown at the distance x/d = 30. While all the meshes perform well in the center cases the two larger meshes perform comparably better in the near and far field regions. Similarly, the temperature is shown in Figure 3.7(b). The small mesh is unable to capture the peak temperature in the near field and overestimates the temperature in the far field. Increasing the cell count from the 20540-cell mesh to the 81880-cell mesh improves the accuracy of the data minimally.

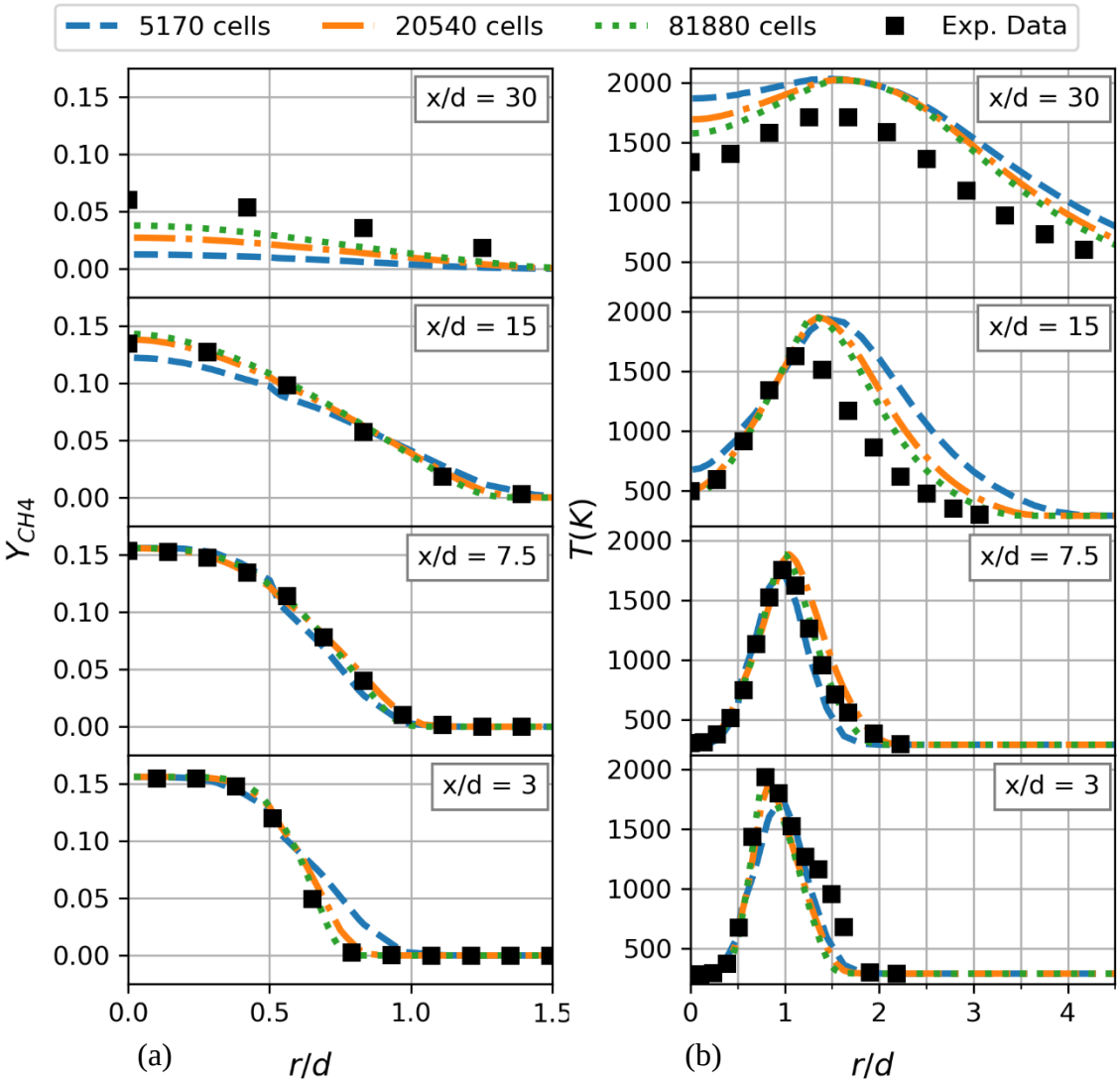

Figure 3.7 - (a) Mass Fraction of CH4 (b) Temperature; effect of the mesh size compared with experimental data.

3.3.2 – Chemical Mechanisms: Computational Time

The computational time of the chemical mechanisms was studied by running the simulation with two different combustion ODE solvers. The percent difference between the outlet and inlet mass and energy was utilized to quantify convergence again. As shown in Figure 3.8, the mass and energy become stable around 15 thousand iterations for the more detailed chemical mechanisms, however, the global mechanism does not converge until around 18 thousand iterations. The converged quantities do not correlate with the number of species or reactions. The final mass difference is within a tenth of a percent for the detailed mechanisms, while the global mechanism (WD2) has a slightly more accurate final value. The final energy balance shows a similar trend, however, the ZG42 energy balance is slightly more accurate than the other detailed mechanism.

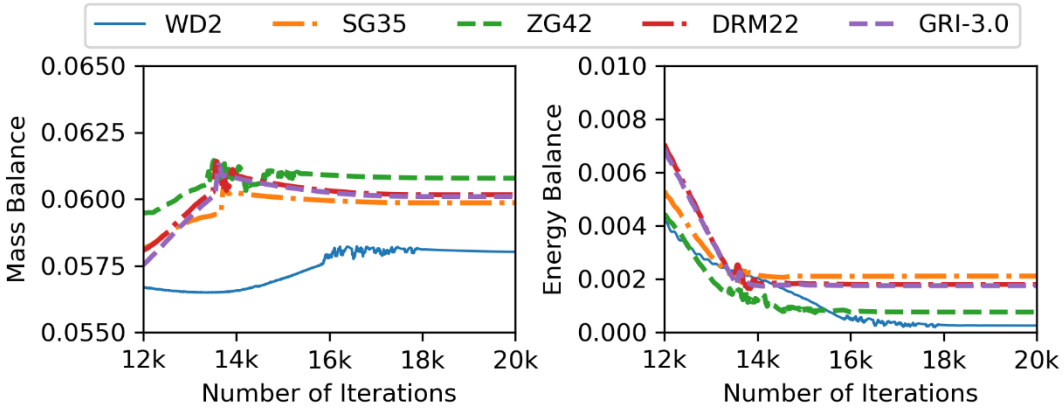

Figure 3.8 – The normalized (left) Mass Balance and (right) Energy Balance as a function of the number of iterations for the various mechanisms

The computational time in CPU hour for the different chemical mechanisms is shown in Figure 3.9. The simulation time increases with increased detail, for the detailed mechanisms. Surprisingly, the WD2 global mechanism computational time was more than the two skeletal mechanisms as seen in Figure 3.9(b). Note that the WD2 mechanism was unstable and did not finish with the SIBS ODE solver and current solver settings. In Figure 3.9(a), the chemical mechanisms as function of the number of reactions was plotted, showing a power relationship

between the number of reactions and the computational time. This matches the theory [44] discussed in Section 3.1 and shown in Figure 3.1.

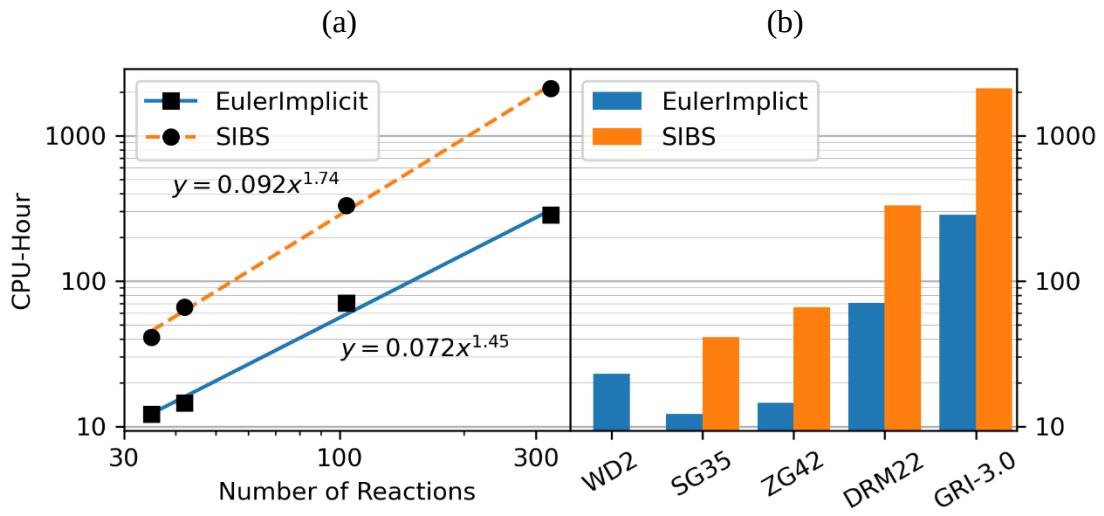

Figure 3.9 – (a) the computational time in CPU hour as a function of the number of reactions with the best fit line excluding WD2 (b) the computational time in CPU hour shown for the various chemical mechanisms.

The computational time for the higher order SIBS solver increases at a higher rate than the EulerImplicit solver. The factor of increase in computational time can be determined by the ratio of the two equations and is shown in Table 3.5. The increase in time for the SIBS model was 3.4 for the smallest mechanisms and 7.5 for the largest mechanism, indicating that higher order models are increasingly costly the larger the mechanism.

Table 3.5 – Computational time and the ratio between the EulerImplicit and SIBS methods

	Computational Time (CPU Hour)		
	EulerImplicit	**SIBS**	**Ratio**
WD2	23.0	-	-
SG35	12.1	41.0	3.4
ZG42	14.6	66.1	4.5
DRM22	70.4	330.3	4.7
GRI-3.0	283	2111	7.5

3.3.3 – Chemical Mechanisms: Experimental Data

CH_4 and O_2, the two primary reactants, were calculated for each mechanism and compared with the experimental data in Figure 3.10. The mass fraction of CH_4, Figure 3.10(a), shows good agreement for all mechanisms for $x/d \leq 15$, while the WD2 mechanism was more accurate for the case $x/d = 30$. The mass fraction of O_2, Figure 3.10(b), diverges from the experimental data and other mechanisms for both WD2 and SG35. At $x/d = 30$, both CH_4 and O_2 are much lower than the experimental values, likely due to the overprediction of combustion in this region.

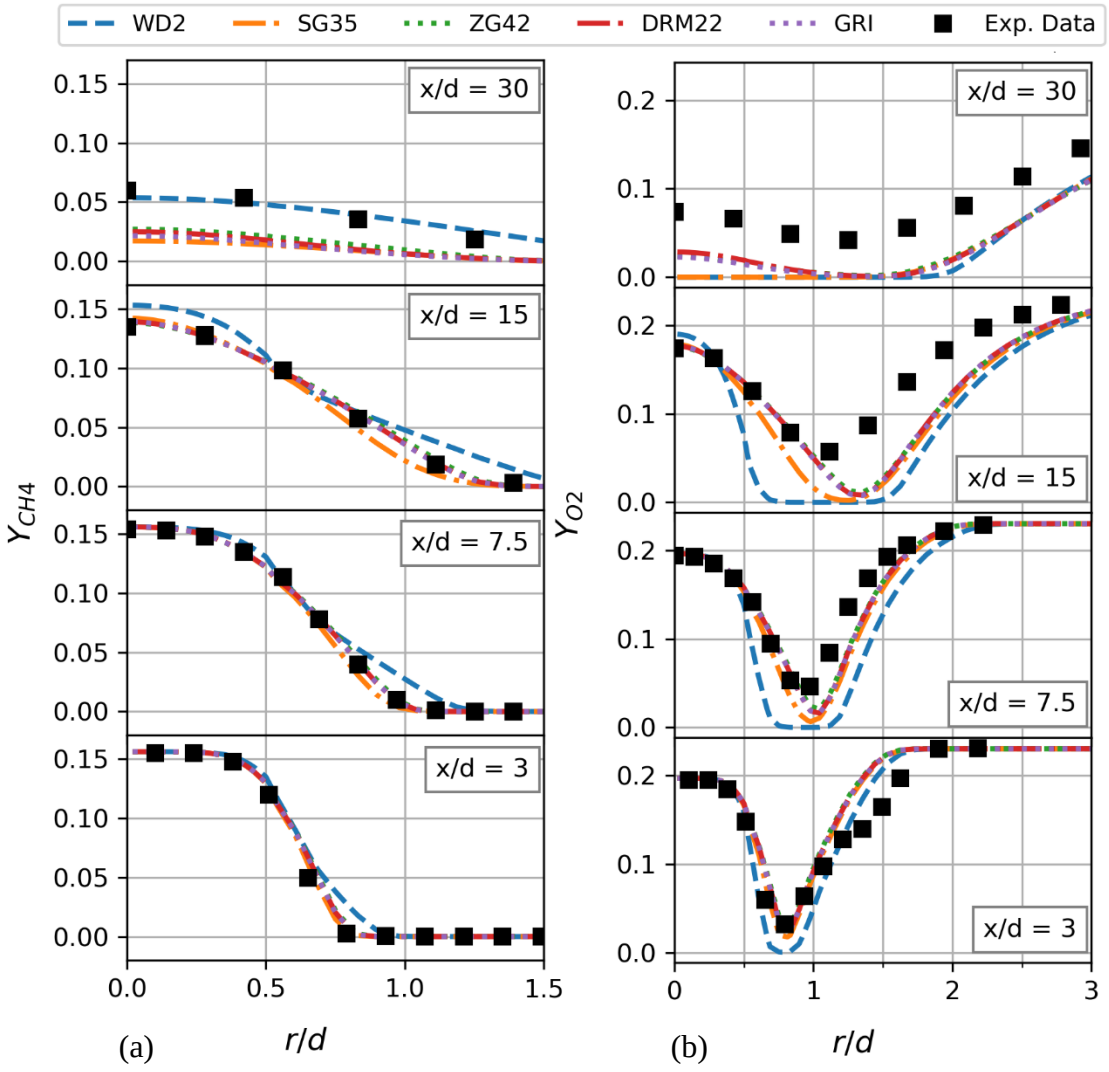

Figure 3.10 - The mass fraction of (a) CH_4 and (b) O_2 compared with experimental data at four locations downstream of the exit, x/d = 3, 7.5, 15, and 30.

H_2O and CO_2, the two primary reaction products, were calculated for each mechanism and compared with the experimental data in Figure 3.11. The mass fraction of H_2O, Figure 3.11(a), and O_2, Figure 3.11(b), are both overpredicted by the WD2 mechanism likely caused by the lack of other oxygen containing species and the under predicting of the mass fraction of CO. The other mechanisms perform similarly for each case, however, SG35 starts to diverge from the other mechanisms and experimental data in the regions farther downstream.

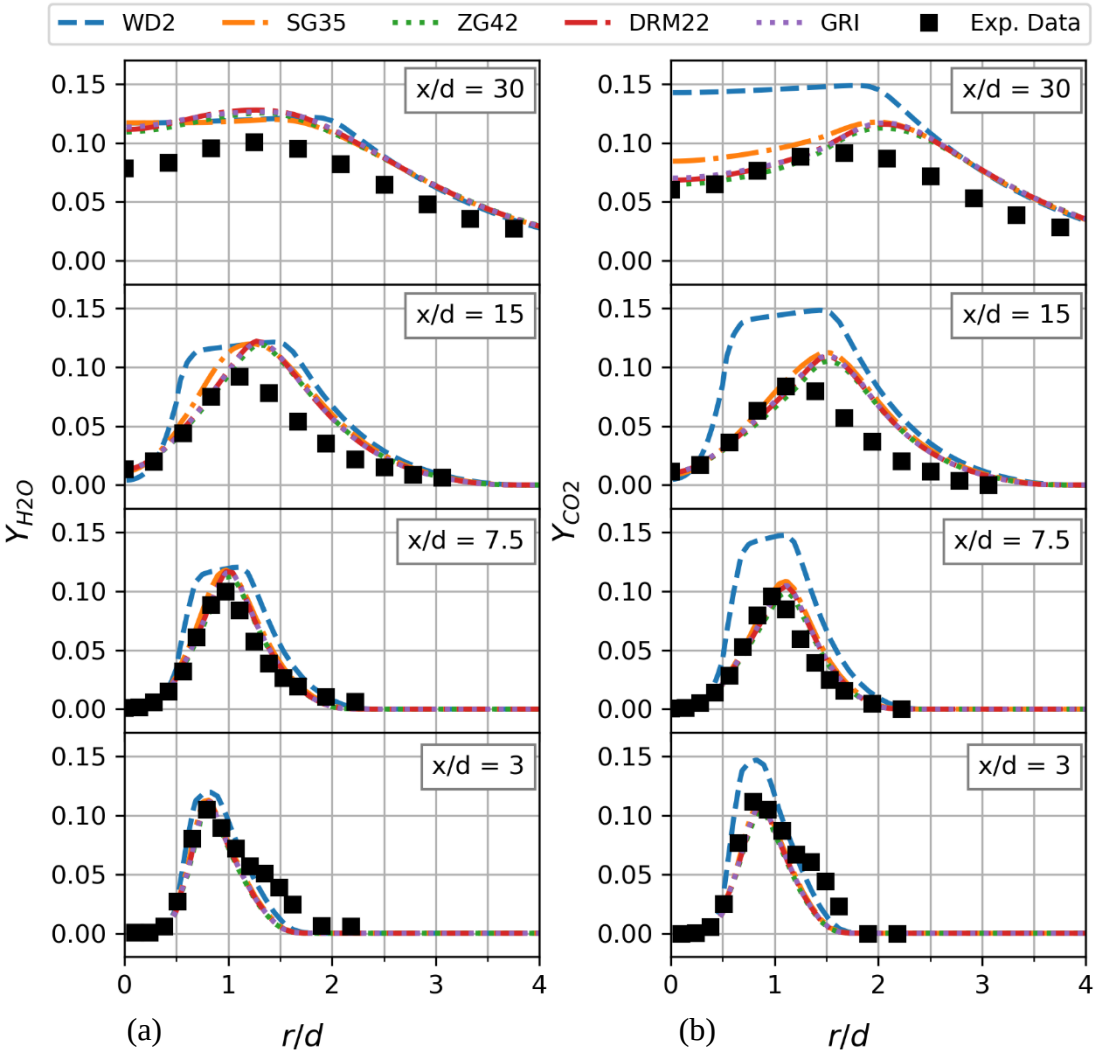

Figure 3.11 - The mass fraction of (a) H_2O and (b) CO_2 compared with experimental data at four locations downstream of the exit, x/d = 3, 7.5, 15, and 30.

Temperature and the z-component velocity were calculated for each mechanism and compared with the experimental data in Figure 3.12. The WD2 mechanism has significantly higher temperatures, Figure 3.12(a), than the other mechanisms. The SG35 temperatures begin to diverge farther away from the jet outlet, while the Z42 temperatures remain comparable to the more detailed mechanisms. All the mechanisms have higher temperatures than the experimental data, which could be a result of neglecting radiation. The z-component velocity, Figure 3.12(b), shows little difference between the mechanisms and the experimental data, except x/d = 15.

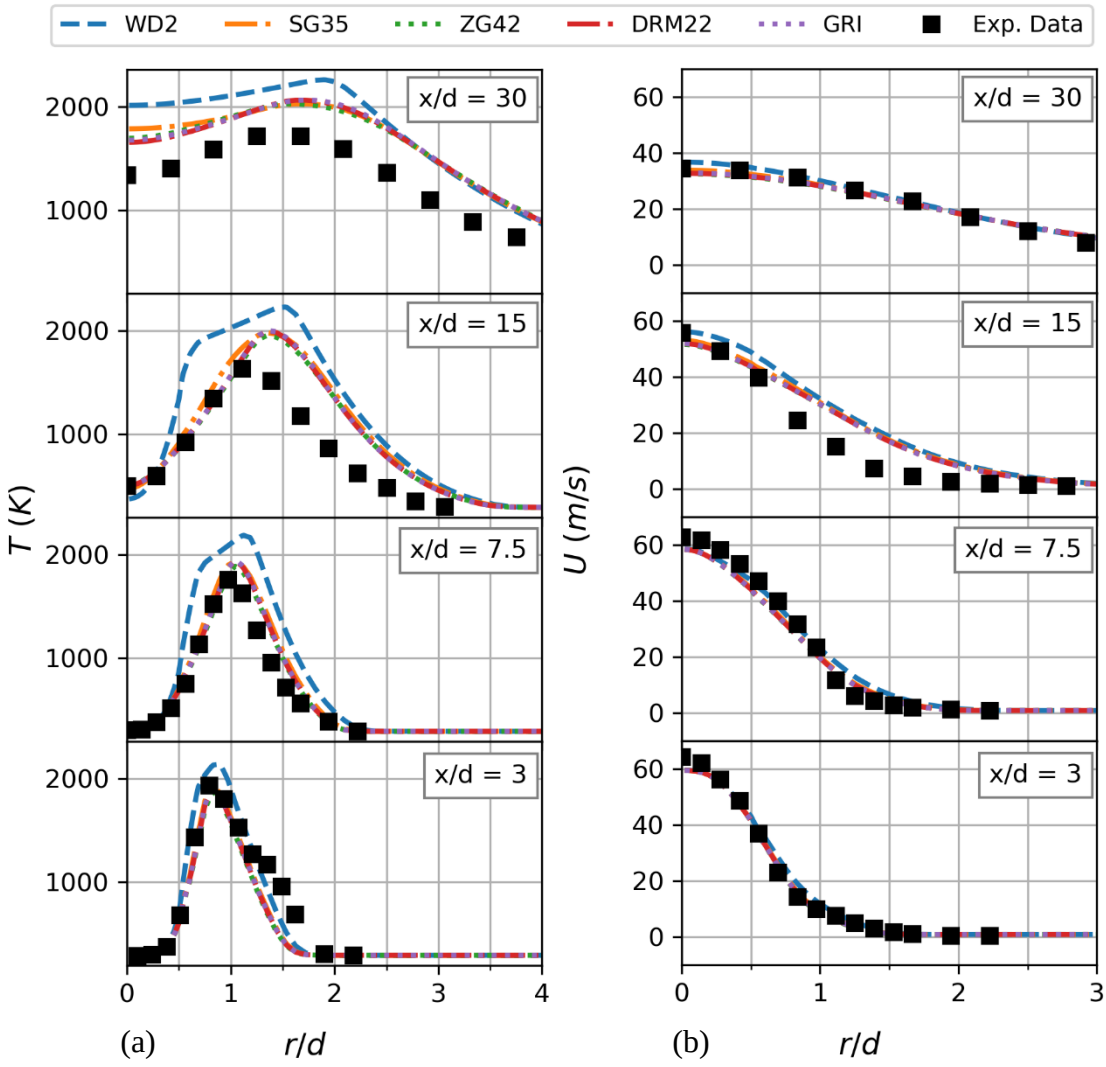

Figure 3.12 - (a) Temperature and (b) z-component velocity compared with experimental data at four locations downstream of the exit, x/d = 3, 7.5, 15, and 30.

3.4 - Conclusions

A comparison study of methane chemical combustion mechanisms was performed with varying levels of complexity. The global mechanism WD2 with 2 reactions was compared with skeletal and detailed mechanisms: SG35, Z42, DRM22, and GRI-30, with 35, 42, 105, and 325 reactions respectively.

The computational cost of the mechanisms was compared. The global mechanism, WD2, was slower than the skeletal mechanisms of similar size. The WD2 mechanism also converged more slowly making the overall simulation time even greater. The skeletal and detailed mechanisms increased in cost with a power relationship to the number of reactions in the mechanism as predicted by theory [44]. The increased order ODE solvers increased the time of the simulation by more than 3 times for the smallest mechanism and over 7 times for the largest, while not improving the results significantly.

The mechanisms were compared to the experimental data to determine accuracy. The WD2 mechanism performed the best for the prediction of CH_4, but significantly differed from the results for all other quantities. The SG35 matched well with the experimental data and other mechanisms but began to diverge in regions farther from the jet exit. The Z42 mechanism compared well with the more detailed mechanisms, while all the mechanisms overpredicted the combustion in the downstream regions.

Based on these results, the Z42 mechanism was the best compromise between computational cost and accuracy. There is no reason to use the global mechanism WD2 since it had reduced accuracy and the computational cost was more than the reduced mechanisms. If speed is the priority the SG35 mechanism will perform well though not as accurately. For more detailed information the GRI-3.0 or other post-processing will be required, particularly for pollutant quantities.

CHAPTER IV

EXPANSION CHAMBER ACOUSTICS VALIDATION

4.1 - Introduction

The expansion chamber silencer is a practical and well tested benchmark for acoustic noise and transmission loss calculation. Finite element analysis has been used to investigate weapon silencers [60] and mufflers using CFD and modal meshing techniques [61]. ANSYS-Fluent, a well-known commercial CFD software, has been used to simulate perforated mufflers using plane wave decomposition [62]. LES and FWH method has been successfully used to study free jet noise and expansion chamber mufflers [63,64] utilizing commercial software. These studies have utilized commercial software to model the expansion chamber, whereas this study would use the free open-source software OpenFOAM. Also, the CFD/FWH method has been utilized for noise prediction in expansion chambers, this method would benefit from a comparison with the acoustic theory for expansion chambers.

A hybrid CFD and acoustic analogy method was used in this study. The CFD was performed utilizing the free open-source software called OpenFOAM. The acoustic analogy was implemented using the free open-source library addition to OpenFoam called *libAcoustics* developed by Epikhin et al. 2015 [34]. They validated the method against the experimental results of the rod-airfoil noise interaction using the Curle analogy. In an earlier study [65], the FWH analogy was also validated with another software using the rod-airfoil interaction. The library has

been used to simulate compressible free jets and compared favorably to experimental data using the FWH method [66,67]. It has also been used to simulate the marine propeller noise [68] and the rotor noise from unmanned aerial vehicles [69,70]. Airfoil generated noise and jet noise has been successfully simulated utilizing the libAcoustics implementation of FWH method. Unfortunately, these previous studies have all focused on exterior flows. The only interior flow has been cavity wall noise [71]. The objective of this study is to validate the libAcoustic library and CFD/FWH method for interior acoustic noise prediction by modeling an expansion chamber silencer and comparing that to plane-wave theory.

4.2 – Computational Methods

4.2.1 - Geometry and Grid

The geometry of the expansion chamber is shown in Figure 4.1 and consists of a pipe with area A_p, an expansion area A_e with a length of L_e, a tail pipe L_t, and a microphone spacing denoted s. In present study the diameter of the pipe was $d_p = 10$ cm, the diameter of the expansion chamber was $d_e = 30$ cm, the length of the expansion chamber was $L_e = 50$ cm, the length of the tail pipe was $L_t = 150$ cm, and the microphone spacing was $s_1 = s_2 = 5$ cm.

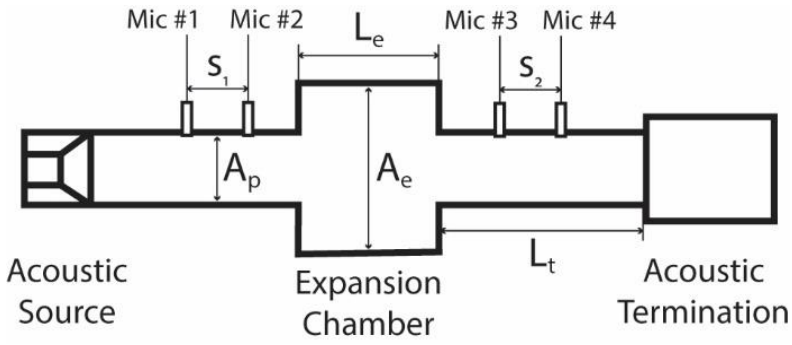

Figure 4.1 – Expansion Chamber impedance tube configuration

Figure 4.2(a) is a 3D rendering of the expansion chamber with the 2D computation region highlighted in yellow. Figure 4.2(b) displays the computational region with computation grid cells visible. The computation region was a 2D wedge configuration. Each cell had an aspect ratio of one and a grid independence study was conducted with dh = 10 mm, 5 mm, 2.5 mm. A 3D mesh was also generated and is shown in Figure 4.3, it had a base height of dh = 5 mm, but due to the circular geometry the exterior cells were stretched.

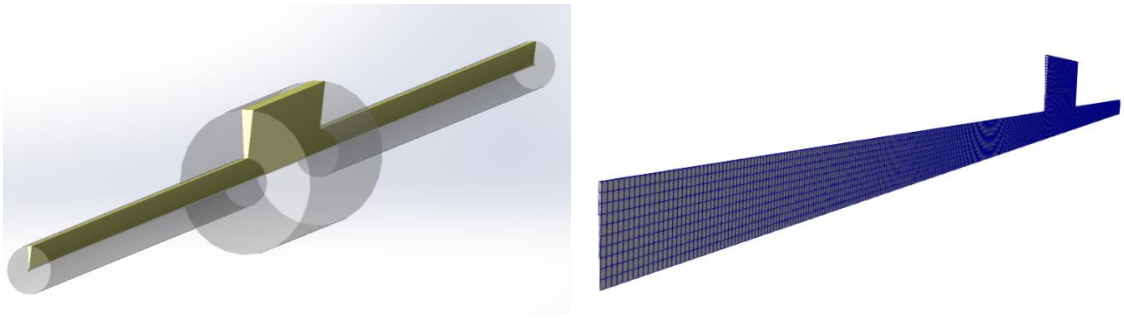

(a) (b)

Figure 4.2 - (a) 3-D rendering of the expansion chamber with computational region highlighted. (b) Computational region of the expansion chamber with grid cells shown at dh = 5 mm.

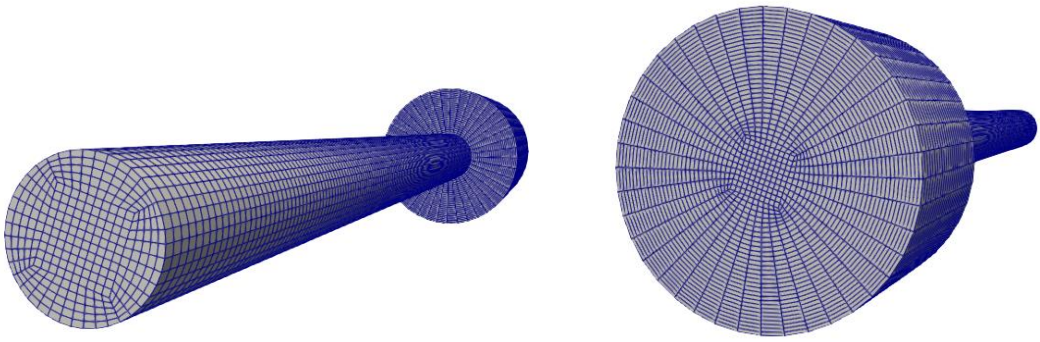

(a) (b)

Figure 4.3 – 3D mesh rendering: (a) inlet of the mesh, (b) clip of the expansion chamber mesh

4.2.2 – Simulation Settings

The solver used for this simulation was *rhoPimpleFoam*, which is a compressible transient flow solver. The first order Euler time scheme was used for transient simulations. The tolerance was set to 10^{-15} to properly resolve the smallest pressure perturbations. The other simulation settings are listed in Table 4.1.

Table 4.1 – Expansion Chamber simulation settings

PIMPLE	nOuterCorrectors nCorrectors	1 2
Solvers	rho|U|h p	PBiCGStab|DILU PBiCGStab|DIC
Numerical Schemes	ddtSchemes gradSchemes divSchemes	Euler linear limitedLinear

The initial and boundary conditions for these quantities are listed in Table 4.2. The temperature was calculated to ensure a speed of sound c = 340 m/s. The outlet of the simulation depended on the anechoic or echoic termination. The acoustic source was simulated with the inlet velocity set to *exprFixedValue* which allowed for an expression dependent on time. The wedge boundary condition defines the edges of the 2D radial mesh but were removed for the 3D mesh.

Table 4.2 – Expansion Chamber simulation boundary conditions

Boundary Field	**Pressure (Pa)**	**Temperature (K)**	**Velocity U (m/s)**
Initial Field	uniform 101325	uniform 287.85	uniform (0 0 0)
outlet	waveTransmissive[1] fixedValue[2]	zeroGradient	waveTransmissive[1] pressureInletOutletVelocity[2]
inlet	zeroGradient	uniform 287.85	exprFixedValue[1]
wall	zeroGradient	zeroGradient	noSlip
cyc1|cyc2 [4]	wedge	wedge	wedge

1. Anechoic termination
2. Echoic termination
3. See Equations 4.1 and 4.2
4. Symmetry plane in 2D simulation

Two methods of sound source simulations were employed. In the first, the inlet velocity was set to a sum of sine waves as shown in Equation 4.1.

$$U = \sum A \sin(2\pi f_i t) \tag{4.1}$$

where A was the amplitude and f_i was the frequency set to a fraction of the speed of sound. The anechoic termination f = [0.40c 0.45c ... 1.05c 1.10c] and for the echoic termination f = [0.30c 0.35c ... 0.85c 0.90c].

In the second, the inlet velocity was given the exponential sine sweep function [72]:

$$U = \sin\left(2\pi f_1 T \frac{(f_2/f_1)^{t/T}-1}{ln(f_2/f_1)}\right) \tag{4.2}$$

where f_1 is the minimum frequency, f_2 is the maximum frequency, and T is the period.

The *libAcoustics* library was utilized for the virtual microphones using the Ffwocs Williams Hawkings (FWH) analogy. Both the Farassat A1 and the GT Formulations were utilized for different conditions and there was no discernable difference between the two since there was no flow or mesh movement. The control volume for all simulations was the exterior wall. The temperature and pressure were set so that the speed of sound would be 340 m/s. The microphones were placed near the wall halfway down the inlet and outlet tubes as described in section 4.1.

4.2.3 – Transmission Loss Calculations

The theoretical transmission loss [73] according to plane wave theory for an anechoically terminated expansion chambers is:

$$TL = 10\log_{10}\left[1 + \frac{1}{4}\left(m - \frac{1}{m}\right)^2 \sin^2 kL_e\right] \tag{4.3}$$

where $m = A_e/A_p$ is the expansion ratio and $k = 2\pi f/c$ is the wave number. The theoretical transmission loss [73] according to plane wave theory for an echoic tailpipe is Eq. 4.4:

$$TL = 10\log_{10}\left[1 + \frac{(m^2-1)^2}{2m^2}\sin^2 kL_e - \frac{m^2-1}{2m}\sin 2kL_t \sin 2kL_e - \frac{m^4-1}{2m^2}\cos 2kL_t \sin^2 kL_e\right] \quad (4.4)$$

It is important to note that the plane-wave theory is accurate only at low sound frequency. The higher frequency sounds have been shown to be a function of the ratio between the diameter and length of the expansion chamber as shown in Figure 4.4 [74,75].

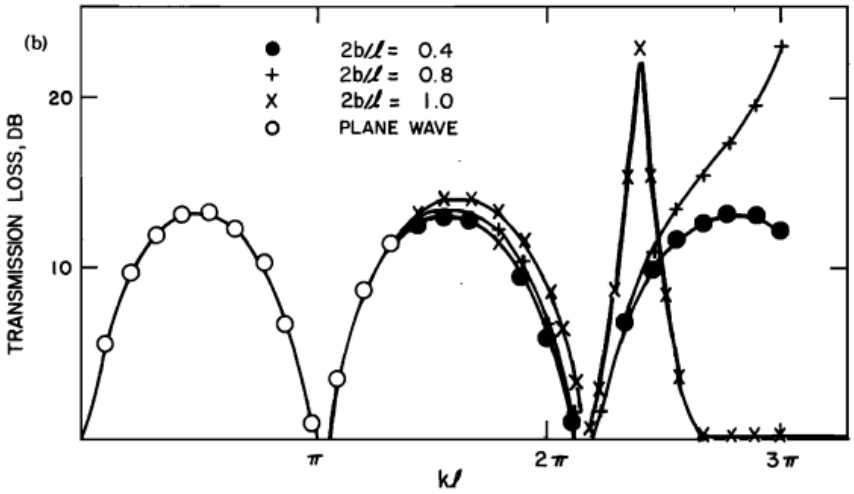

Figure 4.4 – The transmission loss of an expansion chamber silence comparison: El-Sharkawy's method (solid line), finite element analysis, and plane wave theory [74].

The simulated transmission loss was calculated utilizing the two-microphone technique described by Chung and Blaser [76]. Their method defines the acoustic pressures of each microphone as the sum of the incident and reflected components. The convolution integrals are introduced to relate the random acoustic pressures and through mathematic manipulation they found that the complex reflection coefficient at the upstream microphone locations R_u becomes,

$$R_u(f) = [H_{12}(f) - H_i(f)]/[H_r(f) - H_{12}(f)] \quad (4.5)$$

where $H_i, H_r,$ and H_{12} are the impulsive responses corresponding to the incident, reflected, and combined waves evaluated between the two microphone locations.

While assuming plane-wave propagation, no mean flow, and neglecting wall losses, H_i and H_r becomes,

$$H_i(f) = e^{-jks} \tag{4.6}$$

$$H_r(f) = e^{+jks} \tag{4.7}$$

Similarly, the combined incident and reflected waves can be evaluated as

$$H_{12}(f) = \tilde{P}_2(f)/\tilde{P}_1(f) \tag{4.8}$$

where $\tilde{P}(f)$ is the Fourier transform of the pressure signal of the respective microphones.

The transmission loss of the system is defined as the ratio of the incident sound power W_i and the transmitted sound power W_t. These can be shown to be:

$$W_i = S_{uu}A_u/(\rho c|1 + R_u|^2) \tag{4.9}$$

$$W_t = S_{dd}A_d/(\rho c|1 + R_d|^2) \tag{4.10}$$

where A_u is area of the upstream measurement location, A_d is the area of the downstream measurement location, and c is the speed of sound. S_{uu} and S_{dd} are the auto-spectral density of the upstream and downstream measurements respectively.

$$S_{ii}(f) = \frac{1}{T}(\tilde{P}_i(f)\tilde{P}_i^*(f)) \tag{4.11}$$

where T is the period of the measurement and the asterisk denotes a complex conjugate. Using the definition of transmission loss and equations 4.9 and 4.10 the transmission loss can be determined:

$$TL(f) = 20\log_{10}\left|\frac{1+R_d(f)}{1+R_u(f)}\right| - 20\log_{10}\left(\frac{S_{dd}(f)}{S_{uu}(f)}\right)^{\frac{1}{2}} + 10\log_{10}\left(\frac{A_u}{A_d}\right) \tag{4.12}$$

Note that the two-microphone method also assumes plane-wave propagation and therefore does not consider higher acoustic modes. To satisfy this assumption, the measured frequencies should remain below the cut-on frequency of the first higher acoustic node. In radially symmetric configurations, the first radial mode is the cut-on frequency determined by Selamet et al. [77]:

$$f_c = \frac{3.832c}{\pi d_e} \tag{4.13}$$

4.3 – Results and Discussion

4.3.1 – Sum of Sines Method

The *libAcoustics* library calculated the sound pressure data. A portion of this data was plotted for the anechoic termination in Figure 4.5(a) and the echoic termination in Figure 4.5(a). Steady state was determined from this data by visual inspection; a steady pattern is visible in the pressure data plotted in Figure 4.5. Steady state was reached in the anechoic termination after about 7 seconds, and the echoic termination after about 10 seconds.

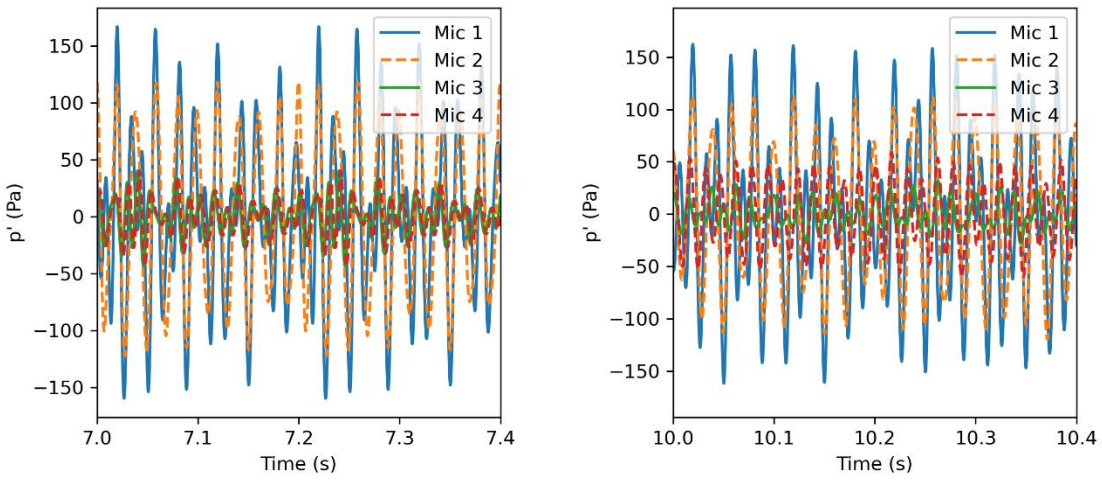

(a) (b)

Figure 4.5 - Pressure signal at the four microphone locations for the (a) Anechoic and (b) Echoic acoustic terminations.

Once steady state has been reached the pressure signal is then transformed into the frequency domain with the Fast-Fourier transform (FFT). The frequency domain pressure signal, plotted in Figure 4.6, demonstrated that the frequencies injected into the simulation were being recognized by the virtual microphones. The frequencies in anechoic terminated simulation were plotted in Figure 4.6(a); frequencies of 40 to 110 Hz in multiples of 5 Hz were injected. The frequencies of the echoic terminated simulations were plotted in Figure 4.6(b); frequencies of 30 to 90 Hz in multiples of 5 Hz were injected. The FFT of the echoic terminated simulation also shows a small discrepancy near the frequency of 50 Hz.

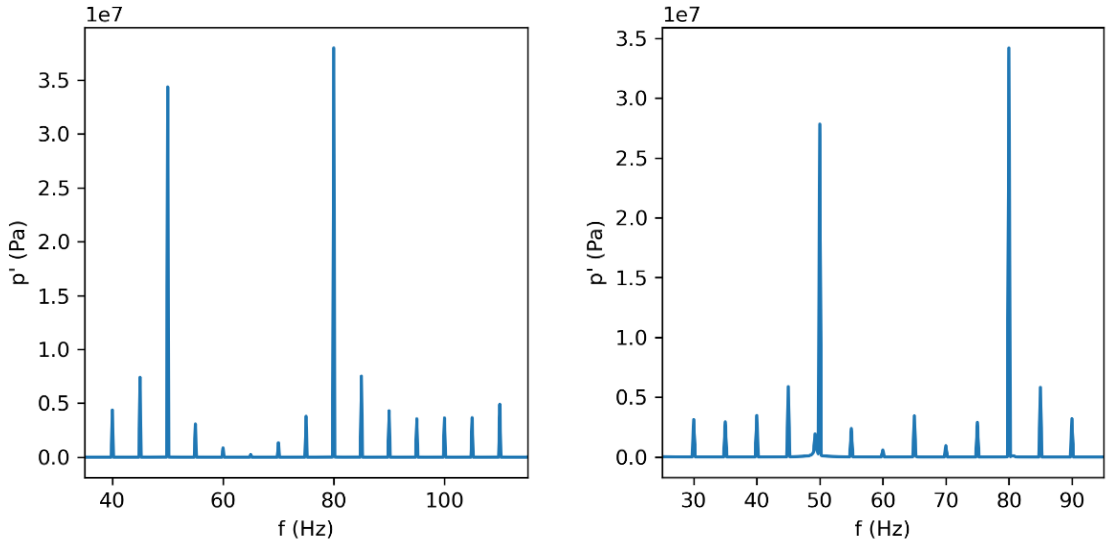

(a) (b)

Figure 4.6 - Fourier transform of the pressure signal for microphone 1 into the frequency domain for (a) anechoic and (b) echoic terminations.

The transmission loss was calculated utilizing the two-microphone method and was compared with the plane-wave theoretical transmission loss. The calculated values showed good agreement with the plane-wave theory as shown in Figure 4.7. The anechoic transmission loss was plotted in Figure 4.7(a). The average absolute error for the anechoic terminated transmission loss was

calculated to be 0.36 dB for dh = 5 mm and dt = 5 μs. The echoic terminated transmission loss was plotted in Figure 4.7(b). The average absolute error for the echoic terminated transmission loss was calculated to be 0.37 dB for dh = 5 mm and dt = 5 μs.

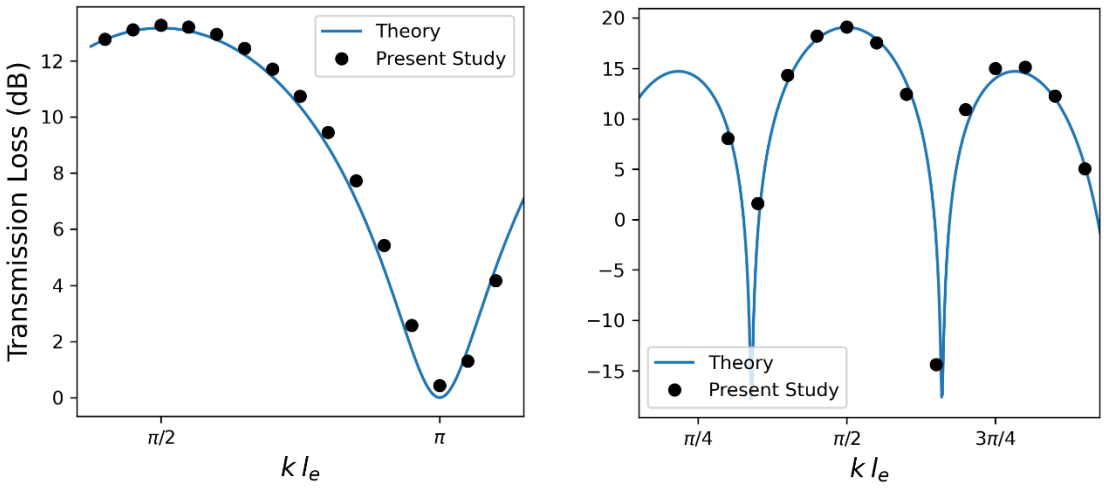

(a) (b)

Figure 4.7 – The transmission loss calculated with the two-microphone method compared with plane wave theory for (a) anechoic termination and (b) echoic termination.

In Figure 4.8(a), the simulated transmission loss of the 3D mesh was compared with the 2D mesh for the anechoic termination. The simulations were performed with dh = 5 mm and dt = 5 μs. The results indicate that the 3D mesh does not greatly impact the acoustic predictions since they are nearly identical to that of the 2D mesh with the same conditions. The average percent difference between the two simulations was 0.58% with an increase in the average absolute error of 0.02 dB. Decreasing the cell height also did not significantly impact the results as shown in Figure 4.8(b). The average absolute error of the results were 0.36 dB, 0.37 dB, and 0.40 dB for the cell heights of dh = 2.5 mm, dh = 5.0 mm, and dh = 10 mm respectively. Based on these results the mesh does not greatly impact the results of the acoustic analogy.

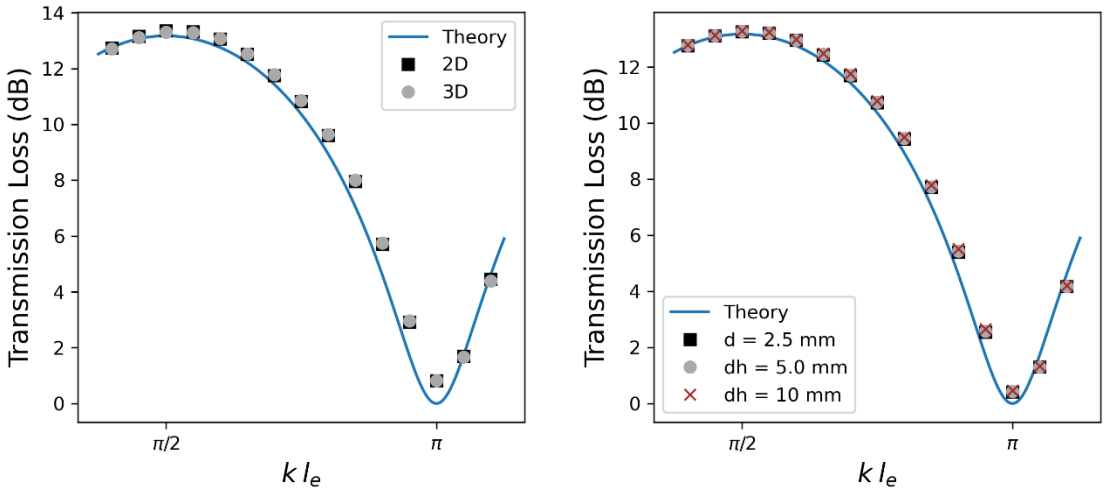

Figure 4.8 – Transmission Loss for an anechoic termination comparing (a) 2D and 3D simulations and (b) the coarseness of the mesh.

4.3.2 – Exponential Sine Sweep Method

Unlike the sum of sines method for the acoustic source, the exponential sine sweep method did not require any time to reach steady state. The period of the sweep was set to one second to ensure a frequency resolution of one Hz. Increasing this period or allowing the sweep to run multiple times did not change the results of the simulation. Therefore, the simulations required much less computational time than that of the sine sum method. The method also was able to resolve all the frequencies between the maximum and the minimum frequencies of the sine sweep.

The effects of the mesh were studied again with the sine sweep and the results for the anechoic mesh are plotted in Figure 4.9. The lower frequencies that were plotted in Figure 4.8(b) again show good agreement with plane wave theory for all cases. However, at the higher frequencies the coarsest mesh begins to have noise, while the other two are relatively similar. They all diverge from the plane wave theory, which is to be expected as described in [74] and shown in Figure 4.3. The effect of changing the simulation from a 2D mesh to a 3D mesh was not seen previously in

Figure 4.8(a). The 3D mesh however does influence the larger frequencies as seen in Figure 4.10. This could, in part, be due to the stretching of the mesh near edge on the mesh. Though the 3D mesh does add some numerical noise the results still match well with that of the 2D mesh.

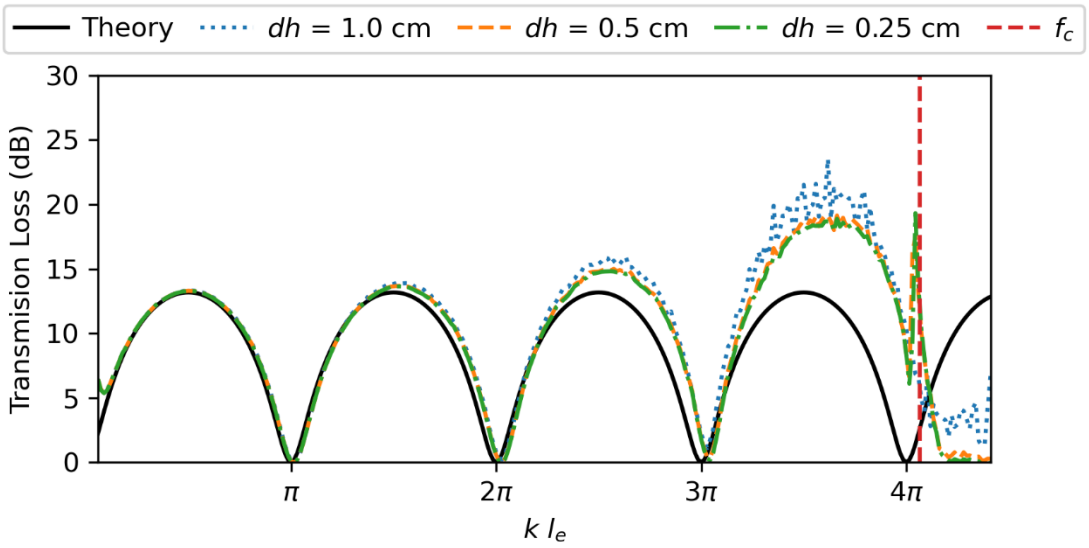

Figure 4.9 – The transmission loss of the anechoic expansion chamber for increasing mesh sizes.

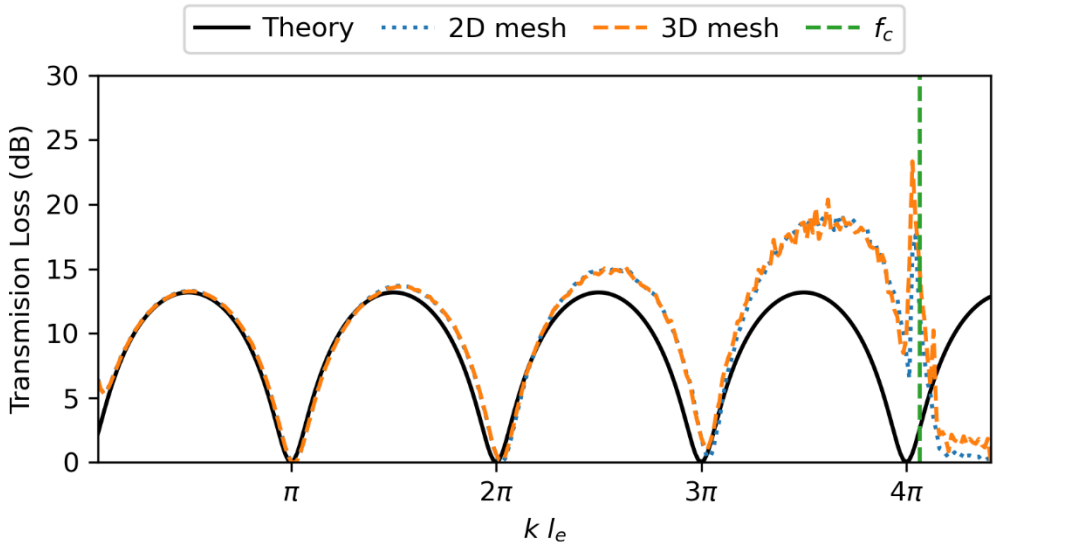

Figure 4.10 - The transmission loss of the anechoic expansion chamber for 3D and 2D mesh.

In Figure 4.11, the transmission loss of the anechoic expansion chamber was compared at different time steps. Decreasing the time step of the simulation significantly changed the results. The decreased time step increased the transmission loss of the simulation by a large amount at higher frequencies. The peaks of the SPL frequency spectrum (Figure 4.12) become smoothed with the smaller time step and the smoothing becomes more pronounced at higher frequencies. The smoothing does not greatly impact the OASP, only causing it to decrease by 2.1%.

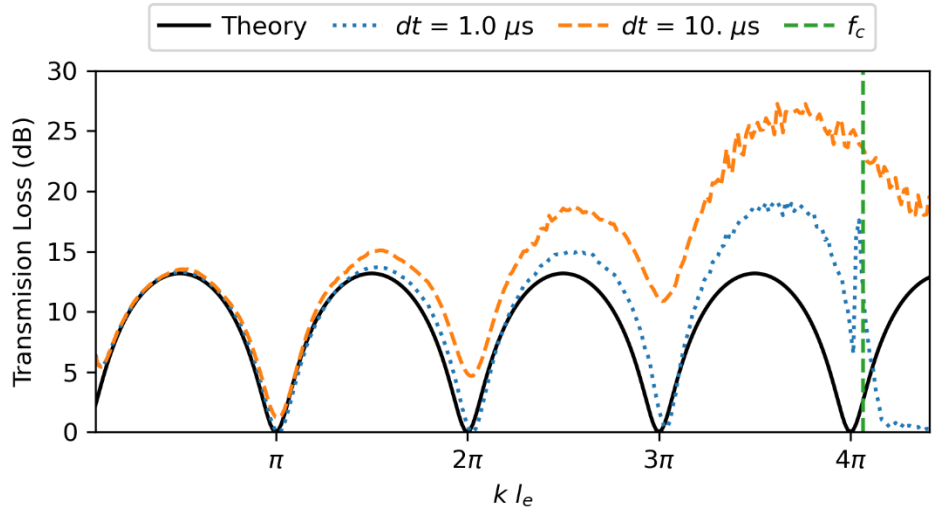

Figure 4.11 – The transmission loss of the anechoic expansion chamber for reduced time step.

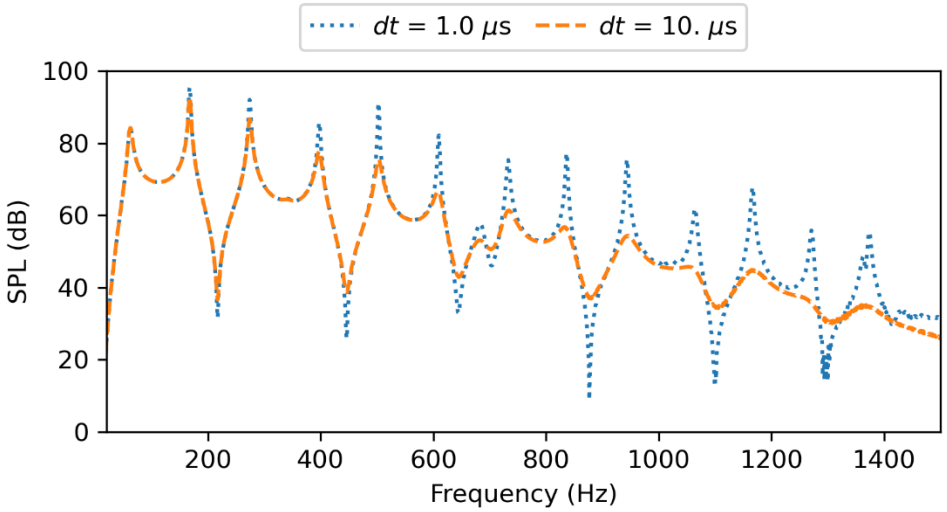

Figure 4.12 – SPL frequency spectrum for the anechoic expansion chamber for reduced time step.

In Figure 4.13, the transmission loss of the echoic expansion chamber was compared at different time steps. A similar occurrence as with the anechoic termination, the decreased time step increased the transmission loss of the simulation significantly. This can be visualized in the SPL frequency spectrum graph shown in Figure 4.14. The peaks of the SPL frequency spectrum are smoothed with increasing frequency. Once again this mainly impacts the transmission loss calculation and the OASPL was only decreased by 2.7%

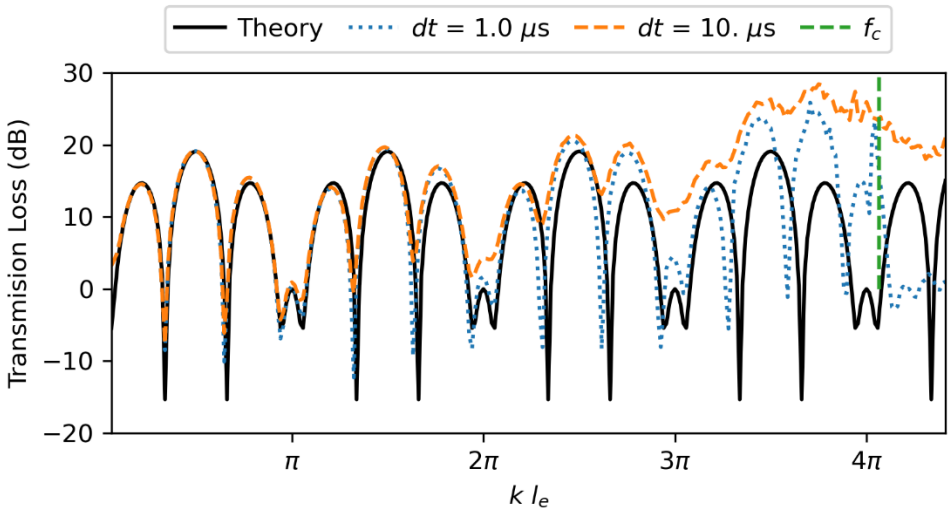

Figure 4.13 - The transmission loss of the anechoic expansion chamber for reduced time step.

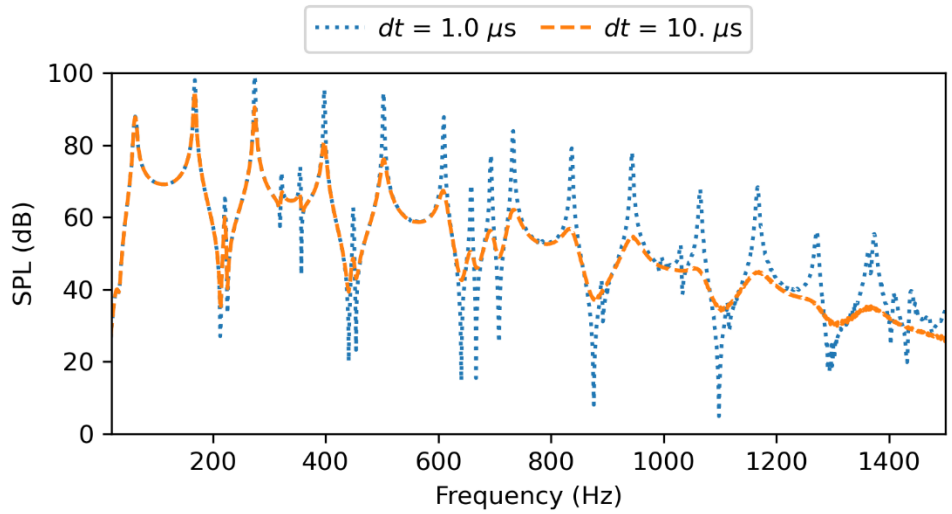

Figure 4.14 – SPL frequency spectrum for the anechoic expansion chamber for reduced time step.

4.4 – Conclusion

The libAcoustics library was utilized to implement the FHW acoustic analogy in an expansion chamber silencer and compared with plane wave theory. The expansion chamber was simulated with both anechoic and echoic terminations. The effect of mesh resolution, 3D vs 2D mesh, and time step on the transmission loss and sound pressure was investigated to determine the validity of the method for enclosed geometries.

Two methods of introducing acoustic perturbations were compared: the sum of sines and the exponential sine sweep method. The sum of sines method required long simulation times to reach steady state, while attempting to calculate the transmission loss before this resulted in incorrect values. The sine sweep method was able to accurately depict the transmission loss after just one second of simulation time resulting in a very large decrease in computational cost. The sine sweep method also resulted in the full frequency spectrum of the transmission loss being able to be resolved, while the sum of sines method could only resolve the inputted frequencies. Both methods accurately calculated the transmission loss but based on computational time and convenience the sine sweep method is superior. Using this method would make both experimental and simulations of expansion chambers and mufflers of other geometries more efficient.

The effect of the mesh was not pronounced on the lower frequencies, while some noise did appear on the higher frequencies. For the cell height, the smallest mesh resulted in a small increase in the calculated transmission loss and oscillations for the largest frequencies. The 3D-mesh had similar magnitude but also experienced oscillations near the cut-on frequency. The effect of the time step was much more pronounced. The increased time step resulted in the transmission loss being less resolved at larger frequencies. The SPL spectrum of the pressure signal was also affected but the OASPL was not changed significantly.

CHAPTER V

LABORATORY SCALE FURNACE ACOUSTICS

5.1 – Introduction

Advancements in combustion techniques such as premixed combustion, improve the efficiency of furnaces and reduce emission. However, premixed combustion had inherent instabilities which leads to increases in the combustion noise. Much of the literature for combustion noise involves jet engines, however small-scale furnaces such as residential heating and hot water units have been neglected. These devices have become increasingly noisy with the adoption of premixed flames and complex heat exchanger designs. Commercially, the noise in these furnaces is often reduced through an iterative design process, however, this is time consuming and costly. With increased availability of computational resources, these methods can be utilized to reduce the cost and time requirements of this process.

Hybrid methods have been implemented previously in OpenFOAM [78,79] and others [80,81] on open flames. Much of the literature for confined flames involves noise prediction in swirl combustors [82-86]. The literature is lacking in low Reynolds number internal flow with combustion. The literature is lacking in noise prediction for low Reynolds number flow with standard flame geometries. Validations of the acoustic analogy method using the FWH method for confined flows are also lacking. This study aims to validate the applicability of a hybrid

CFD/CAA method using the LES/FWH and URANS/FWH method by modeling a laboratory scale furnace in OpenFOAM.

5.2 – Experimental Methods

The experimental setup was designed to deliver premixed CH_4 and air into the burner. The diagram of the setup is shown in Figure 5.1 and photographs of the experiment are shown in Figure 5.2. Shop air was piped to the setup and filtered for particulates and moisture. N_2 was used for purging the system post-combustion to remove any combustible gasses from the setup and for calibrating the Bronkhorst mass flow controllers: 10 L/min for the air and 1 L/min for the CH_4. The mass flow controllers were pre-loaded with the capability for measuring in liters per minute of air and CH_4. The burner was placed in a (1.5 x 2.5 x 0.25) inch square pipe made from stainless steel 304 with rounded corners. The viewing chamber was aluminum with quartz windows. A DSLR camera was placed to record video and photos of the flame. From the base of the viewing chamber to the outlet of the square pipe was 27.5 inches. The burner outlet was a standard Bunsen burner design with stabilizer and was 7 inches from the bottom of the duct.

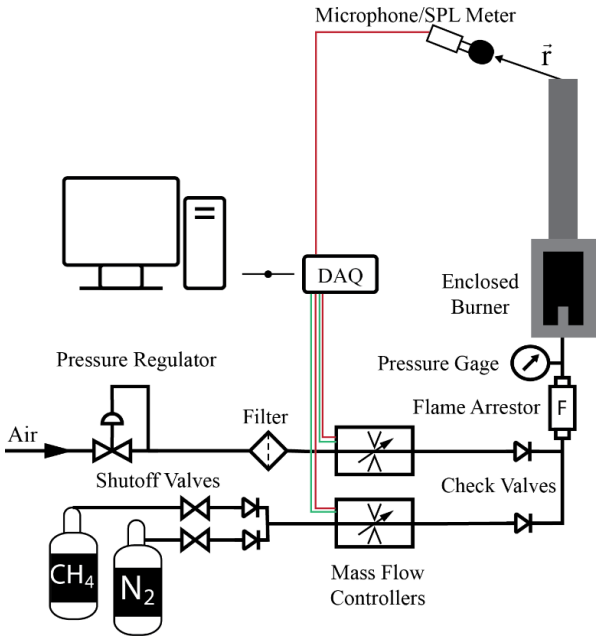

Figure 5.1 – Diagram of the experimental setup.

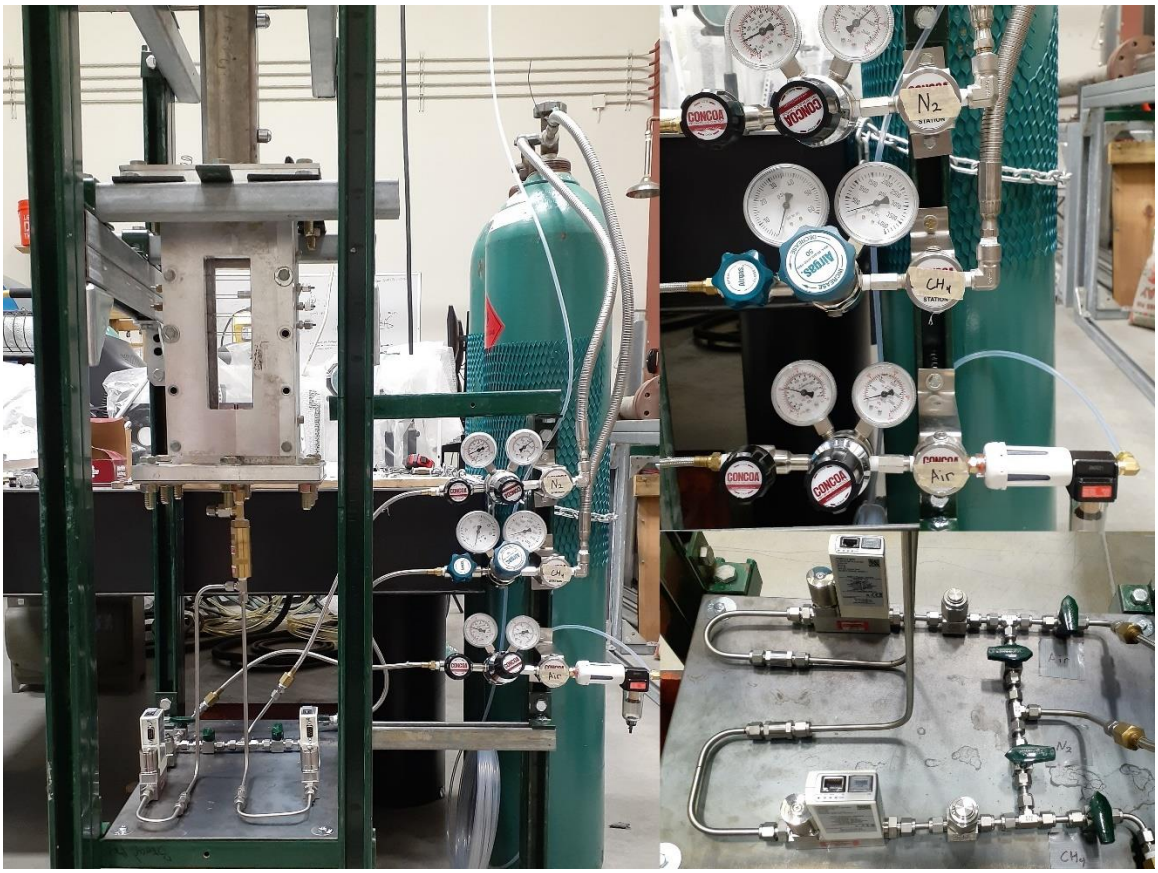

Figure 5.2 – Photographs of the experimental setup

The microphone and SPL meter was placed a distance $\vec{r} = (3, 3, 6)$ inches from the centerline of the outlet plane. The microphone was connected to the computer and simultaneously recorded the sound and measured the SPL spectrum using the REW software [88]. The SPL meter recorded to internal memory then the data was transferred to the computer.

The lean mixture was delivered with equivalence ratio Φ = 1.05, at three different flow rates to determine the effect of flow rate. The flow rates delivered were 4.4 L/min, 7.7 L/min, and 9.9 L/min. The setup was tested at a flow rate of 7.7 L/min for different equivalence ratios: $\Phi = 0.95, \Phi = 1.00, \Phi = 1.05$. The effects of ramping the flow were also investigated at 7.7 L/min flow rate. The flow was tested with no ramping, ramping CH_4 only, ramping air only, and ramping both air and CH_4.

5.3 – Computational Methods

5.3.1 – Burner Geometry and Computation Grid

The standard Bunsen burner stabilizer displayed in Figure 5.3(a) was more complicated than it first may seem. The Bunsen burner had 0.5-inch outer diameter and an approximately 0.44-inch inner diameter with an annular opening around the stabilizer that has an inner diameter of approximately 0.63 inches and an outer diameter of 0.69 inches demonstrated Figure 5.3(b). The annular portion of the Bunsen burner had four small holes located equidistant around the opening as shown in Figure 5.3(c). These openings were estimated based on visual inspection of the burner stabilizer. The Bunsen burner and pipe system was modeled using the SOLIDWORKS modeling suite then inverted to the flow domain demonstrated in Figure 5.3(d).

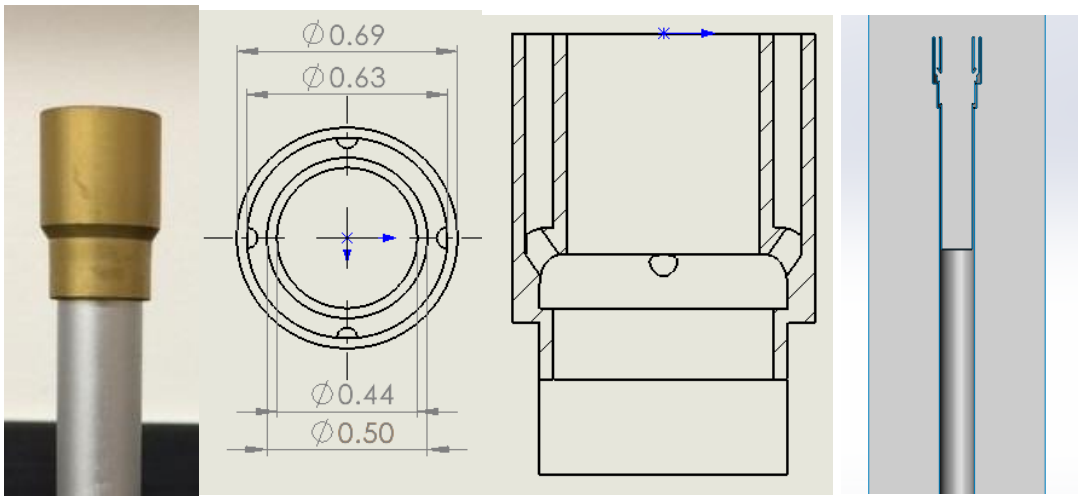

(a) (b) (c) (d)

Figure 5.3 - (a) Image of a Bunsen Burner stabilizer, (b) dimensional drawing of the stabilizer from the top, (c) section view of the Bunsen burner revealing the small openings in the annulus, and (d) the inverted flow domain for the simulation.

The mesh shown in Figure 5.4 had a maximum cell size of 2 mm. A mesh refinement region near the burner outlet with 1 mm cells was used to properly resolve the combustion, wake, and recirculation regions. The cells in the annulus were refined additionally to resolve the geometry

and flow in those regions. Boundary layers were added to the pipe exterior due to the thermal boundary conditions. No boundary layers were placed in the burner since the low reynolds number caused the cells to be small enough to employ the use of wall functions. The mesh had approximately 1.7 million cells.

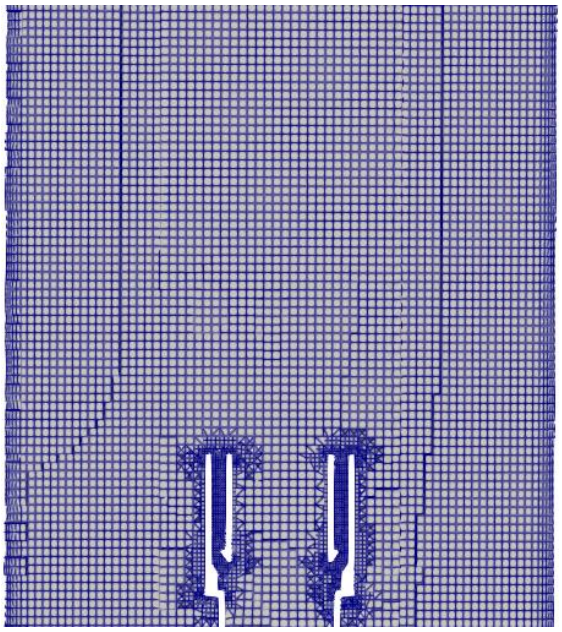

Figure 5.4 - A portion of the mesh surrounding the burner stabilizer.

5.3.2 – Simulation Settings

The solver used for this simulation was *reactingFoam*, which is a compressible transient flow solver. The simulation settings were listed in Table 5.1. The first order Euler time scheme was used for transient simulations. The tolerance was set to 10^{-10} to resolve the small pressure perturbations, but not slow down the simulation too greatly. The time step was set to 10 μs, to ensure stability and reduce computational time.

Table 5.1 – Laboratory scale furnace simulation settings

PIMPLE	nOuterCorrectors	1
	nCorrectors	2
	nNonOrthogonalCorrectors	1
Solvers	rho	diagonal
	U|h|k|epsilon|Yi	PBiCGStab|DILU
	p	PCG|DIC
Numerical Schemes	ddtSchemes	Euler
	gradSchemes	linear
	divSchemes	limitedLinear

The initial and boundary conditions for the simulation are listed in Table 5.2. The species inlet mass fraction was set to match the experimental conditions: $\dot{V} = 7.7$ L/min and $\Phi = 1.05$. The temperature on the pipe was set to simulate the convection heat transfer based on the thermal resistance since the temperature of the mean flow could affect the acoustic predictions.

Table 5.2 – Laboratory scale furnace boundary conditions

Boundary	**Pressure (Pa)**	**Temperature (K)**	**Velocity U (m/s)**
Initial Field	uniform 101325	uniform 300	uniform (0 0 0)
outlet	fixedValue	zeroGradient	pressureInletOutletVelocity
inlet	zeroGradient	uniform 300	flowRateInletVelocity
wallPipe	zeroGradient	externalWallHeatFluxTemperature	noSlip
wallBuner	zeroGradient	zeroGradient	noSlip

The simulation was performed with turbulence modeling since combustion causes fluctuations in the flow. The $k - \epsilon$ closure model was utilized in conjunction with the unsteady Reynolds-averaged Navier stokes (URANS) turbulence model. The WALE [88] (wall-adapting local eddy-viscosity) SGS model for the large-eddy simulations (LES) was used since previous studies have shown good results confined reacting flow [89]. In both cases, wall functions were used for turbulent viscosity ν_t and thermal diffusivity α_t.

The turbulent combustion model used was the Partially Stirred Reactor (PaSR) model with the skeletal reaction mechanism Z42 [42]. The value of the kinematic viscosity air for high temperatures is on the order of 10^{-6} and the kinetic energy and turbulent dissipation can be estimated from the burner geometry. With these and Equation 2.16, $C_{mix} \approx 0.1$.

The *libAcoustics* library was utilized for the virtual microphones with the FWH analogy. The control surface selected was the wall of the pipe. The reference properties used were for ambient air conditions since the microphone was not inside the pipe. The GT-Formulation was used since it reduces the computational cost and the assumptions for stationary microphone and acoustic source are valid in this case.

5.4 – Results and Discussion

5.4.1 – Flame Imaging

The DSLR camera recorded videos of the flames during the combustion process. Once the flames reached their maximum velocity, fluctuations and wrinkling of the flame was observed. The exposure was reduced to capture the flame front. Still images were taken from the videos to demonstrate the flame wrinkling and placed in Figure 5.5. The cause of wrinkling in the flame could be attributed to the interaction with the wall and recirculation regions. There could also be some influence from the upstream turbulence, caused by the inlet of the burner pipe or acoustic interaction.

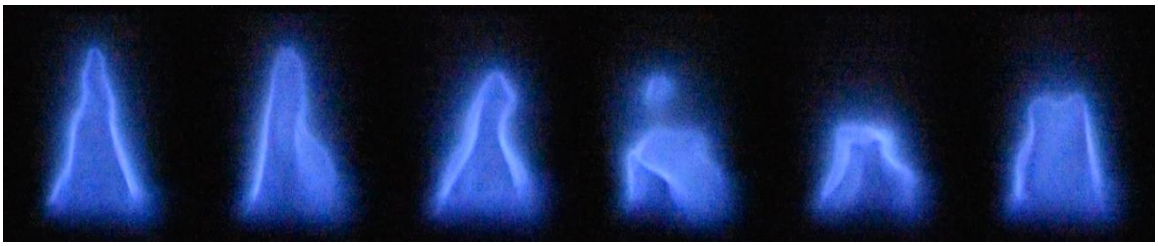

Figure 5.5 - Still images taken from the video recordings demonstrating the wrinkling of the burner's flame cone.

5.4.2 – Measured Noise

After the microphone recorded the sound the free software REW was used to calculate the SPL of the sound. Scientific microphones and SPL meters can be thousands of dollars to purchase, however measurement microphones are available for a fraction of the cost. The UMIK-1 measurement microphone was compared with the Larson & Davis (L&D) SPL meter to determine its accuracy for predicting the SPL frequency spectrum. The SPL 1/3 octave bands are measured by the SPL meter and compared with the measurement microphone in Figure 5.6. The microphone and SPL meter measurements are nearly identical at lower frequency though a small deviation at higher frequencies. The calculated OASPL is within the error (+/- 2 dB) for the measurement microphone. One advantage of the measurement microphone is the ability to visualize the entire frequency spectrum also shown in Figure 5.6.

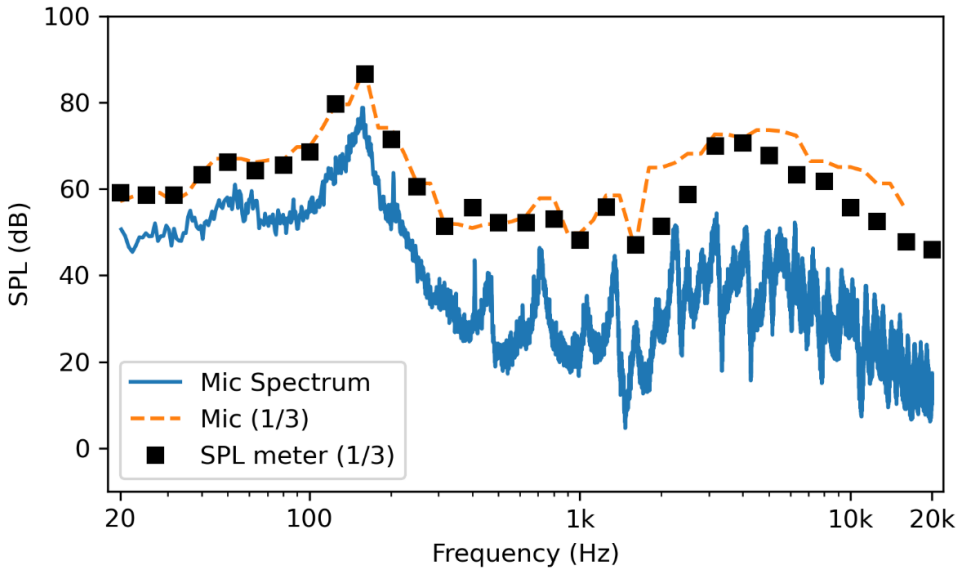

Figure 5.6 - 1/3 octave band measurements: SPL meter and measurement microphone.

The SPL spectrum of the combustion noise, air noise, and the ambient noise at the microphone location was plotted in Figure 5.7. The noise in the lab was significant and may impact the results of the simulation. The noise for the air flow only was higher frequency noise. Part of this noise

could have been caused by upstream flow noise, as well as the noise coming from the piping below the experimental set up. The noise due to combustion was lower frequency, and its peak was around 155 Hz. There were also two smaller amplitude frequencies enhanced by the combustion, at about 450 Hz and 710 Hz. Based on the spectrums, these were likely frequencies caused by the flame while the others were caused by the flow through the tube.

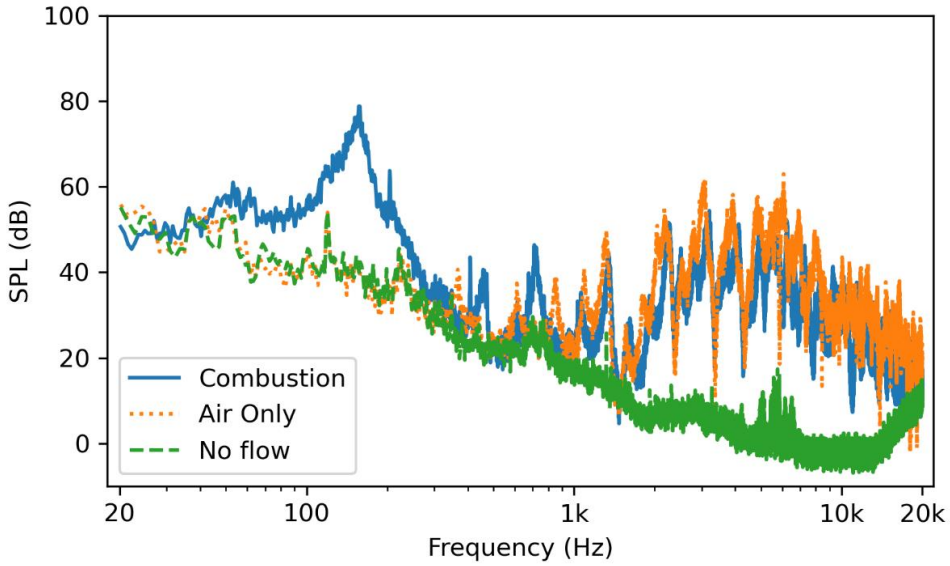

Figure 5.7 – The SPL spectrum for combustion, air flow, and no flow conditions (UMIK-1)

The effect of ramping the flow rate of the gasses was investigated and the 1/3 octave band SPL measured by the SPL meter was plotted as a function of the frequency (Figure 5.8). No ramping and ramping both air and fuel would result in a constant equivalence ratio for the mixture. Ramping air only would result in the mixture being rich when first combusted then transitioning towards lean. Ramping the CH_4 only would result in an even more lean mixture and resulted in ignition taking longer since the mixture started below the flammability limit. Ramping the air and ramping both air and fuel resulted in noise that gradually increased. While the no ramp condition reached full flow rate immediately, once it was reached for the other conditions, the result was the same SPL frequency and amplitudes.

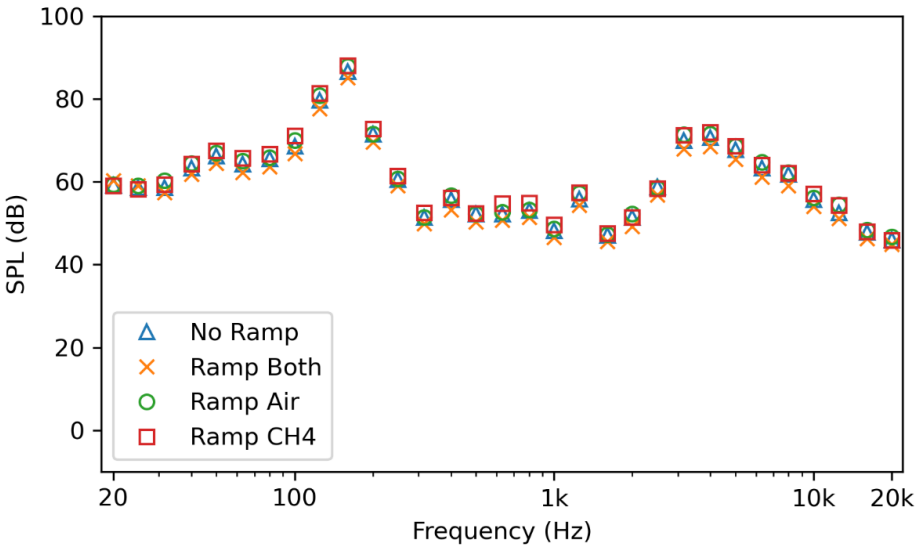

Figure 5.8 - The 1/3 octave band frequencies for the four ramping conditions: no ramp, air and CH_4 ramp, air ramp, and CH_4 ramp. (L&J)

The equivalence ratio was varied from lean to rich and the 1/3 octave bands measured by the UMIK-1 measurement microphone were plotted in Figure 5.9. While there is a slight difference in the peak values, this could be attributed to measurement error. There is no noticeable trend, and the effect of the equivalence ratio is negligible for each condition within the measuring error.

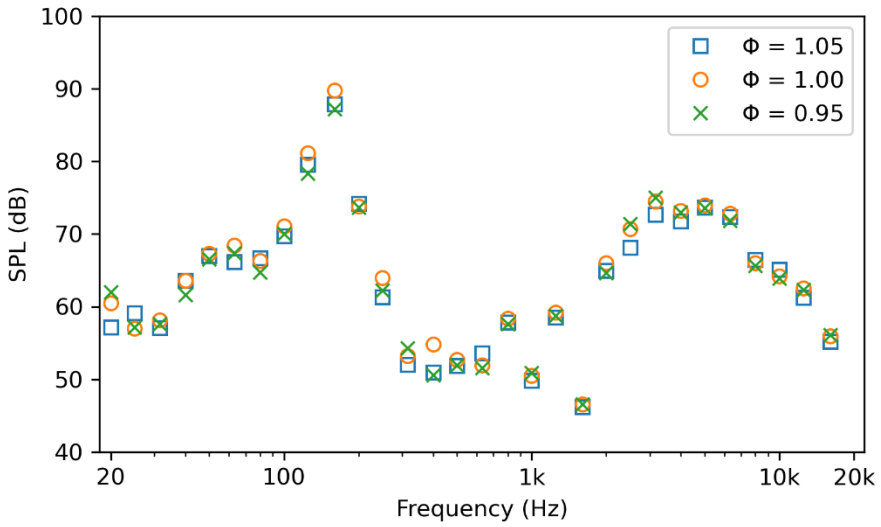

Figure 5.9 - 1/3 octave bands for varying equivalence ratios (UMIK-1)

The effect on the combustion noise of varying the flow rate through the furnace was plotted in Figure 5.10 for the extreme cases of 4.4 L/min and 9.9 L/min. Increasing the flow rate caused proportional increase in the SPL amplitude. The largest peak caused by combustion increased from approximately 69 dB to 84 dB when increasing the flow rate from 4.4 to 9.9 L/min. The peak frequencies also increased with the increase in the flow rate, from around 145 dB at 4.4 L/min to approximately 160 Hz at 9.9 L/min. The smaller peaks due to combustion and air flow show similar trends of increasing frequency and amplitude on the SPL spectrum. The OASPL level also increased linearly with 82 dB, 90 dB, and 95 dB for flow rates of 4.4, 7.7, and 9.9 L/min respectively.

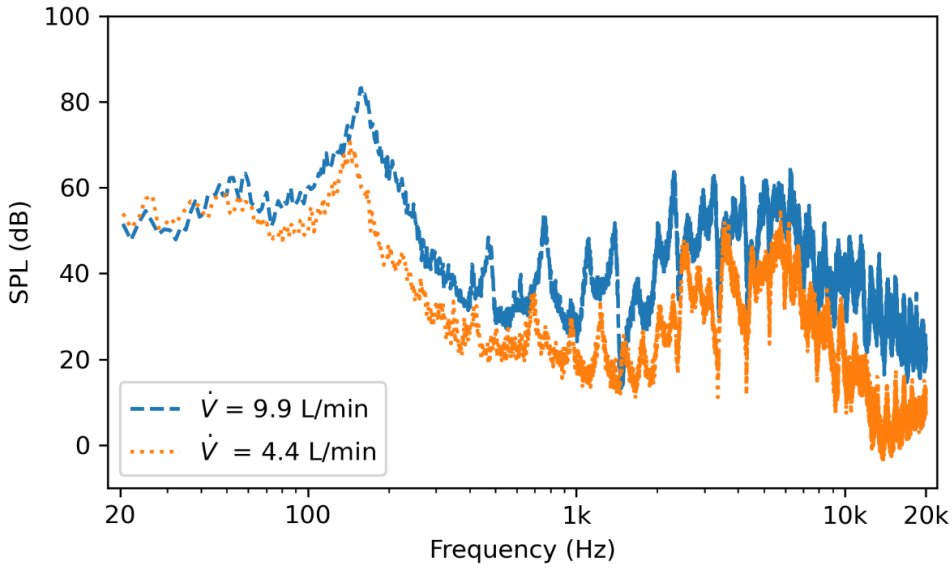

Figure 5.10 - The SPL spectrum for flow rates 4.4 L/min and 9.9 L/min. (UMIK-1)

5.4.3 – Simulation results

The flame was simulated, and the sound pressure was calculated using the *libAcoustics* library FHW acoustic analogy. The sound pressure was transferred to the frequency domain and the amplitude of the sound pressure level was then calculated using python scripts. The SPL frequency spectrum results for both LES and URANS simulation are compared with experimental

data in Figure 5.11. The LES accurately depicted the peak noise from the combustion. The mid-range frequencies were over-predicted, and frequencies of the secondary combustion peaks were shifted to higher frequencies. The large time step likely contributed to the increase in amplitude, causing the resolution of the higher frequencies to be diffused. The geometric differences may have been a factor and the frequencies may have been numerically enhanced by reflections due to boundary conditions. The OASPL of the noise of the LES simulation closely matched the experimental data, 86.7 dB and 86.0 dB respectively. Unfortunately, the URANS simulated noise was significantly under-predicted. Since the mean flow is an averaged quantity, the pressure perturbations that constitute noise are smoothed significantly. It was observed, however, that the overall shape of the URANS simulated noise was similar to the LES simulated noise. When the frequency and the amplitude of the data was 'shifted' (Figure 5.12) by adding 45 dB to the amplitude and subtracting 90 Hz from the frequencies the URANS data performed similarly to the LES predicted values. This indicates that with the proper scaling adjustments the URANS may be used for noise prediction with the FFH analogy.

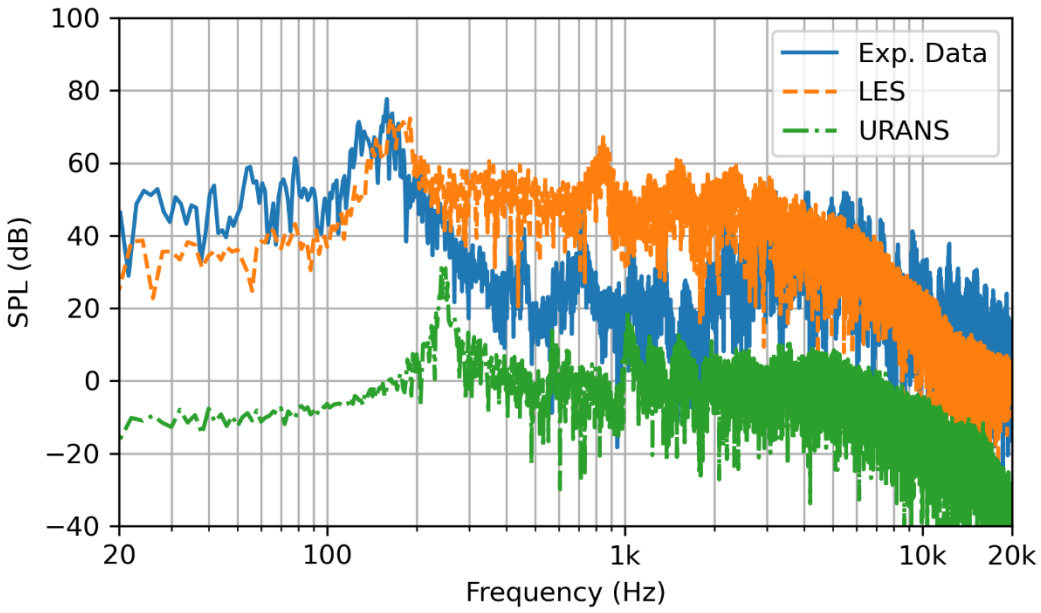

Figure 5.11 - The SPL frequency spectrum for the measured noise and simulated noise

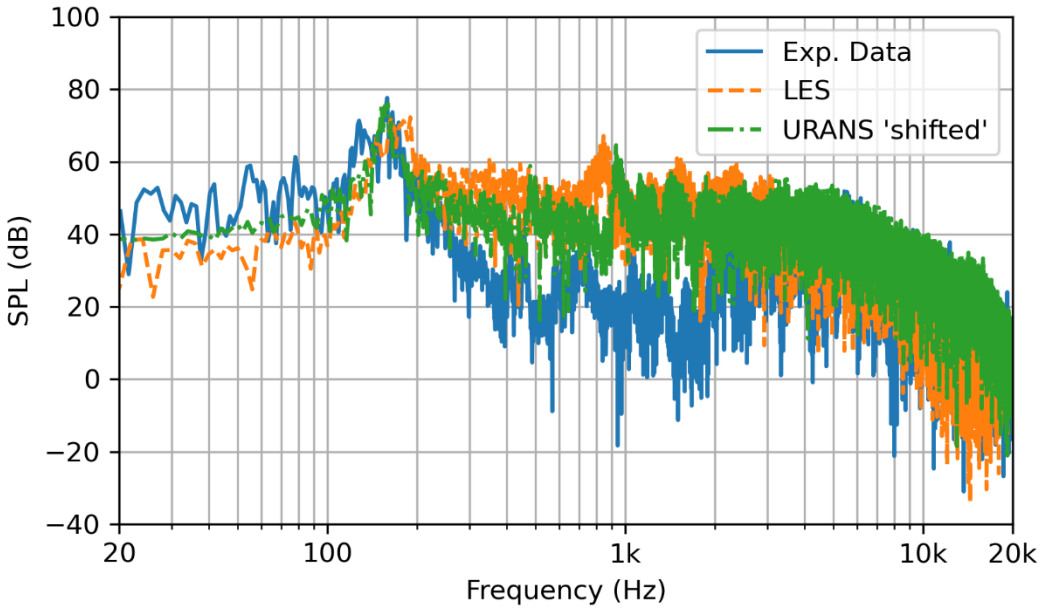

Figure 5.12 - The SPL frequency spectrum for the measured noise and simulated noise with the URANS ‘shifted’ to the amplitude and frequencies of the other signals.

5.5 - Conclusion

A laboratory scale burner was built and tested for various conditions for combustion noise. The DSLR camera captured the wrinkling of the flame, and from the images, the flame height was measured. For noise measurements, the UMIK-1 measurement microphone and J&L SPL meter were compared. The UMIK-1 microphone in combination with the REW software performed well in comparison to the SPL meter. The UMIK-1 has the advantage of being significantly cheaper and the REW software can measure SPL spectrums as well as octave bands. The SPL meter has other features which would make it more advantageous in other circumstances.

Measuring the initial ambient sound found that there was significant noise particularly in the lower frequencies, which may have affected the results. Also, measuring the noise from only air moving in the system demonstrated that it was the main contributor to the high frequency noise. This noise could be the result of the piping below the combustion chamber as well as the flow through the tube.

The equivalence ratio, flow rate, and flow rate ramping noise were all recorded. The equivalence ratio had little effect on the noise, no relationship was discovered. The flow rate of the system was linearly proportional to the SPL and increased the amplitude and frequency of the peaks. Ramping the flow rate, whether both air and CH_4 or either alone, had no discernible effect on the noise of the system. The ramping involves increasing flow rates which was shown to be proportional to the SPL, which may have some effect on a different geometry.

The furnace was simulated using OpenFOAM and the FHW acoustic analogy was implemented with the libAcoustics library. The LES simulation performed well, simulating the amplitude and frequency of the primary combustion peak. The LES overpredicted the mid-range frequencies, but the OASPL was in good agreement with experimental data with a percent difference of 0.8%. The URANS simulation significantly under-predicted the amplitude of the acoustic noise, and the peak frequencies were shifted higher than the experimental data. However, the SPL spectrum was similar in shape, and once 'shifted' performed similarly to the LES simulation. URANS could perform well if a proper scaling technique was determined. URANS/FWH might also be useful in the circumstance such as comparing the OASPL of different geometries, while keeping in mind that the actual OASPL values would be unphysical.

CHAPTER VI

CONCLUSION

6.1 – Summary

A brief overview of Computational Combustion Acoustics (CCA) methods and theory has been given. CCA is a relatively new field, and the computational methods are still being explored. Much is borrowed from CCA's progenitor, computational aeroacoustics, such the use of acoustic analogies. Acoustic problems are difficult to model due to the difference in scales between the acoustic source and the far-field noise. The hybrid CFD acoustic analogy is one solution for dealing with the difference in scales of these problems.

Implementation of the numerical solutions was performed with OpenFOAM, an open-source CFD software. OpenFOAM benefits from the wide community constantly updating and improving functionality. This was taken advantage of here, with the use of *libAcoustics* developed by UniCFD Web-lab, which is not affiliated with OpenFOAM. Descriptions for the implementation of combustion and the *libAcoustics* library were provided for reference. The *libAcoustics* library was validated for confined flow using the expansion chamber silencer and plane wave-theory.

Increased accuracy is required for prediction of combustion noise, but with accuracy generally comes increased computational cost. These simulations can be improved with the use of a chemical mechanism that is both time efficient and accurately models the combustion. Chemical

mechanisms with an increasing number of reactions were compared using the Sandia Flame D. These mechanisms were compared for computational time and the accuracy of results.

Finally, the laboratory scale furnace was built and tested using SPL meter and measurement microphone at a variety of conditions. The effects of equivalence ratio, flow rate, and ramping of the sound pressure amplitude was investigated. The furnace was then simulated using OpenFOAM and libAcoustics to validate the method for confined combustion acoustics.

5.2 – Conclusions

1. The WD2, SG35, Z42, DRM22 and GRI-3.0 combustion mechanisms were compared against the experimental data of the Sandia D Flame. The computational cost of these mechanisms had a power relation to the number reaction as predicted by theory, except for the WD2 mechanism which performed worse than the SG35 and Z42 mechanisms. The Z42 mechanism was determined to be a good compromise between speed and accuracy. It was nearly as accurate as the more complex mechanisms with a fraction of the computational cost.
2. The libAcoustics library was validated using the FHW analogy in an expansion chamber silencer by comparing the simulated data with plane wave theory. The sine-sweep method was determined to be an effective method for simulating the acoustic source. The calculated transmission loss matched well with the plane-wave theory. The effects of the mesh were not as significant as the effect of the time step. Larger time steps smoothed the SPL frequency spectrum, but this did not result in a significantly decreased OASPL.
3. The noise from the laboratory scale furnace was recorded for a variety of conditions. The UMIK-1 microphone was compared to the SPL meter and was found to give sufficient results when used with the REW software. The equivalence ratio and ramping the flow

rate did not significantly alter the SPL spectrum or OASPL. The flow rate had a linear relationship with the SPL amplitude and peak frequencies.

4. A simulation of the furnace was conducted using LES and URANS and the FWH analogy. The LES simulation predicted the combustion peak frequency and amplitude, and the OASPL. The URANS simulation, however, underpredicted the amplitude of the SPL spectrum, but by shifting the values, the URANS was comparable to the LES simulation. This suggests that with the proper scaling techniques developed URANS could be used to predict OASPL, or it might be used for comparing different geometries while delivering unphysical results.

5.3 – Future Work

With the large number of chemical mechanisms being developed, finding a proper mechanism for the current work is difficult. Often many mechanisms may become overlooked or fade into obscurity. Based on the surprising results of Chapter 3, the accuracy and speed of a mechanism is not solely a function of the mechanism complexity. Also, for industrial applications, often the question is not how accurate a mechanism is but rather what mechanism performs well enough without large computational costs? With all this in mind, it would be beneficial for a database to be created for chemical mechanisms. A centralized location for the mechanisms to be stored in a standard format, with the parameters of validity, and relevant literature available. The chemical mechanisms could be rated by their performance in certain categories of literature, allowing researchers to quickly determine the best mechanisms for their application.

The results from Chapter 4 agreed well with plane wave theory, but as predicted by theory and experimentation of higher modal effects diverged at higher frequency. The FFW acoustic analogy predicted the low frequencies well, but it is unclear whether the higher frequencies would be resolved. Comparing the analogy implementation with theory that takes into account higher

modes or experimental data should be performed to ensure that the method is valid for the full range of audible frequencies. An impedance tube experimental setup could be used to further validate the usefulness of the exponential sine sweep method for measuring transmission loss, since the method can be used both experimentally and numerically.

The results from the experimental furnace in Chapter 5 indicate there was ambient noise in the laboratory where the measurements were taken. This noise may have had an unwanted effect on the measurements. In the future, the use of an anechoic chamber would prevent noise from contaminating the acoustic measurements. Also, the flow through the pipes below the furnace could have introduced additional noise. Placing the piping and instrumentation in a soundproof box and adding a silencer to the flow before the burner would prevent noise from these sources. Further the results from Chapter 5 indicate that the URANS method does not accurately predict the SPL amplitudes. However, with further study and experimentation a relationship could be determined that would scale the URANS results with post-processing to the proper levels. This work could provide a method for implementing acoustic prediction while reducing the computational cost requirements.

Many furnaces operate under partially pre-mixed conditions. In the future adding an alternate inlet geometry to accommodate this would allow for testing under these conditions. Other burner geometries such as bluff bodies and rectangular orifices should be tested for their effect on the noise. Adding obstacles to the outlet of the pipe would allow the effects of indirect noise to be observed and would more accurately simulate a hot water heater geometry. It would be beneficial as well to measure the noise from more complex and realistic geometries such as the interaction between multiple burners in a single combustion chamber. Much of recent advances involve combusting hydrogen, or a mixture of hydrogen and methane. Including different fuels such as these would also be an important step. With the current and further validation of the FWH acoustic analogy these experiments might be implemented in OpenFOAM.

REFERENCES

[1] W. C. Strahle, "Combustion noise," *Progress in Energy and Combustion Science*, vol. 4, no. 3, pp. 157–176, 1978.

[2] S. Candel, D. Durox, S. Ducruix, A.-L. Birbaud, N. Noiray, and T. Schuller, "Flame Dynamics and combustion noise: Progress and challenges," *International Journal of Aeroacoustics*, vol. 8, no. 1, pp. 1–56, 2009.

[3] P. Dowling and Y. Mahmoudi, "Combustion noise," *Proceedings of the Combustion Institute*, vol. 35, no. 1, pp. 65–100, 2015.

[4] M. Ihme, "Combustion and engine-core noise," *Annual Review of Fluid Mechanics*, vol. 49, no. 1, pp. 277–310, 2017.

[5] K. Tam, F. Bake, L. S. Hultgren, and T. Poinsot, "Combustion noise: Modeling and prediction," *CEAS Aeronautical Journal*, vol. 10, no. 1, pp. 101–122, 2019.

[6] A. Thomas and G. Williams, "Flame noise: Sound emission from spark-ignited bubbles of combustible gas," *Proceedings of the Royal Society of London. Series A. Mathematical and Physical Sciences*, vol. 294, no. 1439, pp. 449–466, 1966.

[7] I. Hurle, R. Price, T. Sudgen, and A. Thomas, "Sound emission from open turbulent premixed flames," Proceedings of the Royal Society of London. Series A. Mathematical and Physical Sciences, vol. 303, no. 1475, pp. 409–427, 1968.

[8] M. J. Lighthill, "On sound generated aerodynamically I. General theory," *Proceedings of the Royal Society of London. Series A. Mathematical and Physical Sciences*, vol. 211, no. 1107, pp. 564–587, 1952.

[9] M. J. Lighthill, “On sound generated aerodynamically II. turbulence as a source of sound,” *Proceedings of the Royal Society of London. Series A. Mathematical and Physical Sciences*, vol. 222, no. 1148, pp. 1–32, 1954.

[10] P. Dowling, J. E. Ffowcs-Williams, and M. M. Sevik, “Sound and sources of sound,” *Journal of Vibration and Acoustics*, vol. 106, no. 3, pp. 320–320, 1984.

[11] K. W. Tam, “Computational aeroacoustics: An overview of computational challenges and applications,” *International Journal of Computational Fluid Dynamics*, vol. 18, no. 6, pp. 547–567, 2004.

[12] M. Wang, J. B. Freund, and S. K. Lele, “Computational prediction of flow-generated sound,” *Annual Review of Fluid Mechanics*, vol. 38, no. 1, pp. 483–512, 2006.

[13] C. Mathews, N.F. Rekos, R.T Nagel, Combustion noise investigation. Technical Report FAA-RD-77-3, FAA, (1977)

[14] C. Mathews and N. F. Rekos, “Prediction and measurement of direct combustion noise in turbopropulsion systems,” *Journal of Aircraft*, vol. 14, no. 9, pp. 850–859, 1977.

[15] W. E. Zorumski, Aircraft noise prediction program theoretical manual, part 1. Technical Report NASA-TM-83199-PT-1, NASA, (1982)

[16] W. E. Zorumski, Aircraft noise prediction program theoretical manual, part 2. Technical Report NASA-TM-83199-PT-2, NASA, (1982)

[17] T. Poinsot, S. Candel, and A. Trouvé, “Applications of direct numerical simulation to premixed turbulent combustion,” *Progress in Energy and Combustion Science*, vol. 21, no. 6, pp. 531–576, 1995.

[18] H. G. Weller, G. Tabor, H. Jasak, C. Fureby, A tensorial approach to computational continuum mechanics using object-oriented techniques, COMPUTERS IN PHYSICS, VOL. 12, NO. 6, NOV/DEC 1998.

[19] *OpenFOAM*. [Online]. Available: https://www.openfoam.com/. [Accessed: 07-Apr-2022].

[20] "Welcome to paraview," *ParaView*. [Online]. Available: https://www.paraview.org/. [Accessed: 07-Apr-2022].

[21] T. Poinsot and D. Veynante, *Theoretical and numerical combustion*. S.l.: T. Poinsot, 2012.

[22] W. Sutherland, "The viscosity of gases and molecular force," *The London, Edinburgh, and Dublin Philosophical Magazine and Journal of Science*, vol. 36, no. 223, pp. 507–531, 1893.

[23] M. W. Chase, Jr. NIST-JANAF Thermochemical Tables. Washington, DC : New York :American Chemical Society ; American Institute of Physics for the National Institute of Standards and Technology, 1998.

[24] R. J. Kee, F. M. Rupley, E. Meeks, and J. A. Miller, "Chemkin-III: A fortran chemical kinetics package for the analysis of gas-phase chemical and plasma kinetics," 1996.

[25] B. Spalding, "Development of the eddy-break-up model of turbulent combustion," *Numerical Prediction of Flow, Heat Transfer, Turbulence and Combustion*, pp. 194–200, 1983.

[26] B. F. Magnussen and B. H. Hjertager, "On mathematical modeling of turbulent combustion with special emphasis on soot formation and combustion," *Proc. Combust. Inst.*, vol. 16, no. 1, pp. 719–729, 1976.

[27] V. Ertesvag and B.F. Magnussen, "The Eddy Dissipation Turbulence Energy Cascade Model," *Combustion Science and Technology*, vol. 159, no. 1, pp. 213–235, 2000.

[28] N. Gran and B.F. Magnussen, "A numerical study of a bluff-body stabilized diffusion flame. part 2. influence of combustion modeling and finite-rate chemistry," *Combustion Science and Technology*, vol. 119, no. 1-6, pp. 191–217, 1996.

[29] B.F. Magnussen, "THE EDDY DISSIPATION CONCEPT A BRIDGE BETWEEN SCIENCE AND TECHNOLOGY." (2005).

[30] J. Chomiak and A. Karlsson, “Flame liftoff in diesel sprays,” *Symposium (International) on Combustion*, vol. 26, no. 2, pp. 2557–2564, 1996.

[31] P. Nordin, A. Niklas. “Complex Chemistry Modeling of Diesel Spray Combustion.” (2001).

[32] D. Christ, “Simulating the combustion of gaseous fuels.” [Online]. Available: http://www.personal.psu.edu/dab143/OFW6/Training/christ_slides.pdf. [Accessed: 07-Apr-2022].

[33] C. Westbrook and F. Dryer, “Simplified reaction mechanisms for the oxidation of hydrocarbon fuels in flames,” *Combustion Science and Technology*, vol. 27, no. 1-2, pp. 31–43, 1981.

[34] A. Epikhin, I. Evdokimov, M. Kraposhin, M. Kalugin, and S. Strijhak, “Development of a dynamic library for computational aeroacoustics applications using the OpenFOAM Open Source Package,” *Procedia Computer Science*, vol. 66, pp. 150–157, 2015.

[35] N. Curle, “The influence of solid boundaries upon aerodynamic sound,” *Proceedings of the Royal Society of London. Series A. Mathematical and Physical Sciences*, vol. 231, no. 1187, pp. 505–514, 1955.

[36] E. F. Williams and D. L. Hawkings, “Sound generation by turbulence and surfaces in arbitrary motion,” *Philosophical Transactions of the Royal Society of London. Series A, Mathematical and Physical Sciences*, vol. 264, no. 1151, pp. 321–342, 1969.

[37] F. Farassat, G. P. Succi, “A review of propeller discrete frequency noise prediction technology with emphasis on two current methods for time domain calculations”, 1980, Journal of Sound and Vibration, 71(3), 399-419

[38] I. E. Garrick. and E. W. Watkins, “A Theoretical Study of the Effect of Forward speed on the Free Space Sound Pressure Field Around Helicopters,” Tech. Rep. TR-1198, NACA, 1954.

[39] G. A. Brès, F. Pérot, and D. Freed, “A Ffowcs Williams - Hawkings solver for lattice-boltzmann based computational aeroacoustics,” *16th AIAA/CEAS Aeroacoustics Conference*, 2010.

[40] “Unicfdlab - overview,” *GitHub*. [Online]. Available: https://github.com/unicfdlab. [Accessed: 07-Apr-2022].

[41] S. Faramawy, T. Zaki, and A. A.-E. Sakr, “Natural gas origin, composition, and processing: A Review,” *Journal of Natural Gas Science and Engineering*, vol. 34, pp. 34–54, 2016.

[42] “Statistical Review of World Energy: Energy Economics: Home,” *bp global*. [Online]. Available: https://www.bp.com/en/global/corporate/energy-economics/statistical-review-of-world-energy.html. [Accessed: 07-Apr-2022].

[43] N. Zettervall, C. Fureby, and E. J. Nilsson, “Evaluation of chemical kinetic mechanisms for methane combustion: A review from a CFD Perspective,” *Fuels*, vol. 2, no. 2, pp. 210–240, 2021.

[44] T. Lu and C. K. Law, “Toward accommodating realistic fuel chemistry in large-scale computations,” *Progress in Energy and Combustion Science*, vol. 35, no. 2, pp. 192–215, 2009.

[45] J. Curran, “Developing detailed chemical kinetic mechanisms for fuel combustion,” *Proceedings of the Combustion Institute*, vol. 37, no. 1, pp. 57–81, 2019.

[46] P. Zhang, I. G. Zsély, V. Samu, T. Nagy, and T. Turányi, “Comparison of methane combustion mechanisms using shock tube and rapid compression machine ignition delay time measurements,” *Energy & Fuels*, vol. 35, no. 15, pp. 12329–12351, 2021.

[47] S. Laguillo, J. S. Ochoa, and A. Ortiz, “Chemical reaction mechanisms assessment for simulation of methane combustion in domestic gas cooking burners,” *Energy & Fuels*, vol. 33, no. 9, pp. 9171–9183, 2019.

[48] F. Delic, “Three-Dimensional Numerical Simulation of Combustion in a Jet Engine,” thesis, 2019.

[49] D. A. Lysenko, I. S. Ertesvåg, and K. E. Rian, “Numerical simulations of the Sandia Flame D using the Eddy dissipation concept,” *Flow, Turbulence and Combustion*, vol. 93, no. 4, pp. 665–687, 2014.

[50] H. Kadar, “Modelling Turbulent Non-Premixed Combustion in Industrial Furnaces,” thesis, 2015.

[51] K. M. Pang, et al. “Development and validation of a local time stepping-based PaSR solver for combustion and radiation modeling.” (2013).

[52] R. S. Barlow and J. H. Frank, “Effects of turbulence on species mass fractions in methane/Air Jet Flames,” *Symposium (International) on Combustion*, vol. 27, no. 1, pp. 1087–1095, 1998.

[53] H. Frank and R. S. Barlow, “Simultaneous Rayleigh, Raman, and LIF measurements in turbulent premixed methane-air flames,” *Symposium (International) on Combustion*, vol. 27, no. 1, pp. 759–766, 1998.

[54] TNF Workshop, http://www.ca.sandia.gov/TNF, R. Barlow, Eds., Sandia National Laboratories

[55] D. Smoke and V. Giovangigli, “Formulation of the premixed and nonpremixed test problems,” *Reduced Kinetic Mechanisms and Asymptotic Approximations for Methane-Air Flames*, pp. 1–28, 1991.

[56] A. Larsson, N. Zettervall, T. Hurtig, E. J. Nilsson, A. Ehn, P. Petersson, M. Alden, J. Larfeldt, and C. Fureby, “Skeletal methane–air reaction mechanism for large eddy simulation of turbulent microwave-assisted combustion,” *Energy & Fuels*, vol. 31, no. 2, pp. 1904–1926, 2017.

[57] Kazakov and M. Frenklach, http://combustion.berkeley.edu/gri-mech/

[58] G. P. Smith, D. M. Golden, M. Frenklach, N. W. Moriarty, B. Eiteneer, M. Goldenberg, C. T. Bowman, R. K. Hanson, S. Song, W. C. Gardiner, Jr., V. V. Lissianski, and Z. Qin http://combustion.berkeley.edu/drm/

[59] G. Bader and P. Deuflhard, "A semi-implicit mid-point rule for stiff systems of ordinary differential equations," *Numerische Mathematik*, vol. 41, no. 3, pp. 373–398, 1983.

[60] H. Arslan, M. Ranjbar, E. Secgin, and V. Celik, "Theoretical and experimental investigation of acoustic performance of multi-chamber reactive silencers," *Applied Acoustics*, vol. 157, p. 106987, 2020.

[61] J. Wu, X. J. Wang, and H. B. Tang, "Transmission loss prediction on a single-inlet/double-outlet cylindrical expansion-chamber muffler by using the modal meshing approach," *Applied Acoustics*, vol. 69, no. 2, pp. 173–178, 2008.

[62] D. Zhu and Z. L. Ji, "Transmission loss prediction of reactive silencers using 3-D time-domain CFD approach and plane wave decomposition technique," *Applied Acoustics*, vol. 112, pp. 25–31, 2016.

[63] E. Liu, S. Peng, and T. Yang, "Noise-silencing technology for upright venting pipe jet noise," *Advances in Mechanical Engineering*, vol. 10, no. 8, p. 168781401879481, 2018.

[64] H. Guo, Y. S. Wang, F. Zhu, N. N. Liu, and C. Yang, "Multi-field coupling prediction for improving aeroacoustic performance of muffler based on Les and Fw-H acoustic analogy methods," *International Journal of Aeroacoustics*, vol. 20, no. 3-4, pp. 414–436, 2021.

[65] D. Casalino, M. Jacob, and M. Roger, "Prediction of rod-airfoil interaction noise using the ffowcs-williams-hawkings analogy," *AIAA Journal*, vol. 41, no. 2, pp. 182–191, 2003.

[66] A. Epikhin, M. Kraposhin, and K. Vatutin, "The numerical simulation of compressible jet at low Reynolds number using openfoam," *E3S Web of Conferences*, vol. 128, p. 10008, 2019.

[67] A. Epikhin and M. Kraposhin, “Prediction of the free jet noise using quasi-gas dynamic equations and acoustic analogy,” *Lecture Notes in Computer Science*, pp. 217–227, 2020.

[68] J. Kimmerl, V. Krasilnikov, K. Koushan, P. Mertes, L. Savio, M. Felli, M. Abdel-Maksoud, U. Göttsche, and N. Reichstein, (2019). Analysis Methods and Design Measures for the Reduction of Noise and Vibration Induced by Marine Propellers. 10.18154/RWTH-CONV-240003.

[69] M. Heydari, H. Sadat, and R. Singh, “A computational study on the aeroacoustics of a multi-rotor unmanned aerial system,” *Applied Sciences*, vol. 11, no. 20, p. 9732, 2021.

[70] R. R. Mankbadi, S. O. Afari, and V. V. Golubev, “High-fidelity simulations of noise generation in a propeller-driven unmanned aerial vehicle,” *AIAA Journal*, vol. 59, no. 3, pp. 1020–1039, 2021.

[71] P. Łojek, I. Czajka, A. Gołaś, and K. Suder-Dębska. (2021). Influence of the elastic cavity walls on cavity flow noise. Vibrations in Physical Systems. 32. 2021. 10.21008/j.0860-6897.2021.1.09.

[72] S. Müller, and P. Massarani, "Transfer-Function Measurement with Sweeps," J. Audio Eng. Soc., vol. 49, no. 6, pp. 443-471, (2001 June.).

[73] K. A. Sallam, A. S. Sabry, M. A. Serag-Eldin, and M. A. Fouad, “International Congress on Fluid Dynamics and Propulsion.”

[74] I. El-Sharkawy and A. H. Nayfeh, “Effect of an expansion chamber on the propagation of sound in circular ducts,” *The Journal of the Acoustical Society of America*, vol. 63, no. 3, pp. 667–674, 1978.

[75] Y.H. Kim, J. W. Choi, and B. D. Lim, “Acoustic characteristics of an expansion chamber with constant mass flow and steady temperature gradient (theory and numerical simulation),” *Journal of Vibration and Acoustics*, vol. 112, no. 4, pp. 460–467, 1990.

[76] Y. Chung and D. A. Blaser, “Transfer function method of measuring in-duct acoustic properties. I. Theory,” *The Journal of the Acoustical Society of America*, vol. 68, no. 3, pp. 907–913, 1980.

[77] A. Selamet, N. S. Dickey, and J. M. Novak, “A time-domain computational simulation of acoustic silencers,” *Journal of Vibration and Acoustics*, vol. 117, no. 3A, pp. 323–331, 1995.

[78] F. Zhang, P. Habisreuther, H. Bockhorn, H. Nawroth, and C.O. Paschereit, (2013). On prediction of combustion generated noise with the turbulent heat release rate. *Acta Acustica United with Acustica*, *99*(6), 940–951. https://doi.org/10.3813/aaa.918673

[79] F. Zhang, P. Habisreuther, M. Hettel, and H. Bockhorn, (2012). Numerical computation of combustion induced noise using compressible Les and hybrid CFD/CAA methods. *Acta Acustica United with Acustica*, *98*(1), 120–134. https://doi.org/10.3813/aaa.918498

[80] F. Flemming, A. Sadiki, J. Janicka, (2007). Investigation of Combustion Noise using a Les/CAA Hybrid Approach. *Proceedings of the Combustion Institute*, *31*(2), 3189–3196. https://doi.org/10.1016/j.proci.2006.07.060

[81] W. Zhao, and S. H. Frankel, (2001). Numerical simulations of sound radiated from an axisymmetric premixed reacting jet. *Physics of Fluids*, *13*(9), 2671–2681. https://doi.org/10.1063/1.1386940

[82] M. Merk, W. Polifke, R. Gaudron, M. Gatti, C. Mirat, and T. Schuller, (2018). Measurement and simulation of combustion noise and dynamics of a confined Swirl Flame. *AIAA Journal*, *56*(5), 1930–1942. https://doi.org/10.2514/1.j056502

[83] C. F. Silva, M. Merk, T. Komarek, and W. Polifke, (2017). The contribution of intrinsic thermoacoustic feedback to combustion noise and resonances of a confined turbulent premixed flame. *Combustion and Flame*, *182*, 269–278. https://doi.org/10.1016/j.combustflame.2017.04.015

[84] M. Merk, R. Gaudron, C. Silva, M. Gatti, C. Mirat, T. Schuller, and W. Polifke, (2019). Prediction of combustion noise of an enclosed flame by simultaneous identification of Noise Source and flame dynamics. *Proceedings of the Combustion Institute*, *37*(4), 5263–5270. https://doi.org/10.1016/j.proci.2018.05.124

[85] M. Merk, S. Jaensch, C. Silva, and W. Polifke, (2018). Simultaneous identification of transfer functions and combustion noise of a turbulent flame. *Journal of Sound and Vibration*, *422*, 432–452. https://doi.org/10.1016/j.jsv.2018.02.040

[86] C.F. Silva, M. Leyko, F. Nicoud, and S. Moreau, (2013). Assessment of combustion noise in a premixed swirled combustor via large-eddy simulation. *Computers & Fluids*, *78*, 1–9. https://doi.org/10.1016/j.compfluid.2010.09.034

[87] J. Mulcahy. (2022). REW room acoustics and Audio Device Measurement and Analysis Software. Room EQ Wizard Room Acoustics Software. Retrieved April 10, 2022, from https://www.roomeqwizard.com/

[88] M. Germano, U. Piomelli, P. Moin, and W.H. Cabot (1991). A dynamic subgrid-scale eddy viscosity model. Physics of Fluids A: Fluid Dynamics, 3(7), 1760–1765. https://doi.org/10.1063/1.857955

[89] N. Arya, and A. De (2019). Effect of grid sensitivity on the performance of wall adapting SGS models for Les of Swirling and separating–reattaching flows. Computers & Mathematics with Applications, 78(6), 2035–2051. https://doi.org/10.1016/j.camwa.2019.03.038

VITA

Andrew J. Williamson

Candidate for the Degree of

Master of Science

Thesis: SIMULATION OF COMBUSTION NOISE OF PREMIXED FLAMES IN OPENFOAM

Major Field: Mechanical and Aerospace Engineering

Biographical:

Education:

Completed the requirements for the Master of Science in Mechanical Engineering at Oklahoma State University, Stillwater, Oklahoma in May 2022.

Completed the requirements for the Bachelor of Science in Mechanical Engineering at Oklahoma State University, Stillwater, Oklahoma in May 2019.

Experience:

Graduate Research Assistant for Oklahoma State University, School of Mechanical and Aerospace Engineering 2019 to 2022

Graduate Teaching Assistant for Oklahoma State University, School of Mechanical and Aerospace Engineering 2019 to 2020

Undergraduate Research Assistant for Oklahoma State University, School of Mechanical and Aerospace Engineering 2018 to 2019

Professional Memberships:

Student Member of the American Society for Mechanical Engineers

Student Member of the American Society of Heating, Refrigerating and Air-Conditioning Engineers